

1 **Sensitivity of cloud phase distribution to cloud microphysics and**
2 **thermodynamics in simulated deep convective clouds and SEVIRI**
3 **retrievals**

4 Cunbo Han^{1,2}, Corinna Hoose¹, Martin Stengel³, Quentin Coopman⁴, Andrew Barrett¹

5

6 1. Institute of Meteorology and Climate Research (IMK-TRO), Karlsruhe Institute of
7 Technology, Karlsruhe, Germany

8 2. State Key Laboratory of Tibetan Plateau Earth System, Environment and
9 Resources (TPESER), Institute of Tibetan Plateau Research, Chinese Academy
10 of Sciences, Beijing, China

11 3. Deutscher Wetterdienst (DWD), Offenbach, Germany

12 4. Department of Atmospheric and Oceanic Sciences, McGill University, Montreal,
13 Canada

14

15

16

17

18

19 Correspondence to: Cunbo Han (cunbo.han@hotmail.com) and Corinna Hoose
20 (corinna.hoose@kit.edu)

21

22

23 **Abstract:**

24 The formation of ice in clouds is an important process in mixed-phase clouds, and
25 the radiative properties and dynamical developments of clouds strongly depend on
26 their partitioning between liquid and ice phases. In this study, we investigated the
27 sensitivities of the cloud phase to ice-nucleating particle (INP) concentration and
28 thermodynamics. Moreover, passive satellite retrieval algorithms and cloud products
29 were evaluated to identify whether they can detect cloud microphysical and
30 thermodynamical perturbations. Experiments were conducted using the ICOSahedral
31 Nonhydrostatic model (ICON) at the convection-permitting resolution of about 1.2 km
32 on a domain covering significant parts of central Europe, and were, compared to two
33 different retrieval products based on SEVIRI measurements. We selected a day with
34 multiple isolated deep convective clouds, reaching a homogeneous freezing
35 temperature at the cloud top. The simulated cloud liquid pixel fractions were found to
36 decrease with increasing INP concentration both within clouds and at the cloud top.
37 The decrease in cloud liquid pixel fraction was not monotonic but was stronger in
38 high INP cases. Cloud-top glaciation temperatures shifted toward warmer
39 temperatures with increasing INP concentration by as much as 8 °C. Moreover, the
40 impact of INP concentration on cloud phase partitioning was more pronounced at the
41 cloud top than within the cloud. Moreover, initial and lateral boundary temperature
42 fields were perturbed with increasing and decreasing temperature increments from 0
43 to +/-3K and +/-5K between 3 and 12 km. Perturbing the initial thermodynamic state
44 was also found to affect the cloud phase distribution systematically. However, the
45 simulated cloud-top liquid pixel fraction, diagnosed using radiative transfer
46 simulations as input to a satellite forward operator and two different satellite remote
47 sensing retrieval algorithms, deviated from one of the satellite products regardless of
48 perturbations in the INP concentration or the initial thermodynamic state for warmer
49 sub-zero temperatures, while agreeing with the other retrieval scheme much better,
50 in particular for the high INP and high convective available potential energy (CAPE)
51 scenarios. Perturbing the initial thermodynamic state, which artificially increases the
52 instability of the mid- and upper-troposphere, brought the simulated cloud-top liquid
53 pixel fraction closer to the satellite observations, especially in the warmer mixed-
54 phase temperature range.

55

删除了: are

删除了: are

删除了: are

删除了: i

删除了: i

删除了: i

删除了: are

删除了: i

删除了: s

删除了: brings

66 **Keywords:** Mixed-phase clouds, deep convection, INP, thermodynamics, satellite
67 forward operator, remote-sensing retrieval algorithms

68

69 **Key points:**

- 70 1. Cloud properties are retrieved using a satellite forward operator and remote
71 sensing retrieval algorithms with ICON simulations as input. To our knowledge,
72 it is the first time this approach has been used to retrieve cloud phase and other
73 microphysical variables.
- 74 2. Glaciation temperature shifts towards a warmer temperature with increasing
75 INP concentration both within the cloud and at the cloud top. Initial
76 thermodynamic states affect the cloud phase distribution significantly as well.
- 77 3. Simulated cloud-top liquid pixel fraction matches the satellite observations in
78 the high INP and high CAPE scenarios.

79

80 **1. Introduction**

81 In the temperature range between 0 and -38°C, ice particles and supercooled liquid
82 droplets can coexist in mixed-phase clouds. Mixed-phase clouds are ubiquitous in
83 Earth's atmosphere, occurring at all latitudes from the poles to the tropics. Because
84 of their widespread nature, mixed-phase processes play a critical role in the life cycle
85 of clouds, precipitation formation, cloud electrification, and the radiative energy
86 balance on both regional and global scales ([Korolev et al., 2017](#)). Deep convective
87 clouds are always mixed-phase clouds, and their cloud tops reach the homogeneous
88 freezing temperature, -38°C, in most cases. Despite the importance of mixed-phase
89 clouds in shaping global weather and climate, microphysical processes for mixed-
90 phase cloud formation and development are still poorly understood, especially ice
91 formation processes. It is not surprising that the representation of mixed-phase
92 clouds is one of the big challenges in weather and climate models ([McCoy et al.,
93 2016](#); [Korolev et al., 2017](#); [Hoose et al., 2018](#); [Takeishi and Storelvmo, 2018](#); [Vignon
94 et al., 2021](#); [Zhao et al., 2021](#)).

95
96 The distribution of cloud phase has been found to impact cloud thermodynamics and
97 Earth's radiation budget significantly ([Korolev et al., 2017](#); [Matus and L'Ecuyer,
98 2017](#); [Hawker et al., 2021](#)). The freezing of liquid droplets releases latent heat and
99 hence affects the thermodynamic state of clouds. Moreover, distinct optical
100 properties of liquid droplets and ice particles exert different impacts on cloud's
101 shortwave and longwave radiation. Simulation and observation studies reported that
102 the cloud phase in the mixed-phase temperature range of convective clouds is
103 influenced by aerosol and plays a significant role in the development into deeper
104 convective systems ([Li et al., 2013](#); [Sheffield et al., 2015](#); [Mecikalski et al., 2016](#)).
105 Observational studies reveal that the cloud phase distribution is highly temperature-
106 dependent and influenced by multiple factors, for example, cloud type and cloud
107 microphysics ([Rosenfeld et al., 2011](#); [Coopman et al., 2020](#)). Analyzing passive
108 satellite observations of mixed-phase clouds over the Southern Ocean, [Coopman et
109 al. \(2021\)](#) found that cloud ice fraction increases with increasing cloud effective
110 radius. Analysis of both passive and active satellite datasets reveals an increase in
111 supercooled liquid fraction with cloud optical thickness ([Bruno et al., 2021](#)).

112

113 A number of in-situ observations of mixed-phase clouds have been made in the past
114 several decades, covering stratiform clouds ([Pinto, 1998](#); [Korolev and Isaac, 2006](#);
115 [Noh et al., 2013](#)) and convective clouds ([Rosenfeld and Woodley, 2000](#); [Stith et al.,
116 2004](#); [Taylor et al., 2016](#)). Aircraft-based observations of mixed-phase clouds
117 properties reveal that the frequency distribution of the ice water fraction has a U-
118 shape with two explicit maxima, one for ice water fraction smaller than 0.1 and the
119 other for ice water fraction larger than 0.9, and the frequency of occurrence of mixed-
120 phase clouds is approximately constant when the ice water fraction is in the range
121 between 0.2 and 0.5 ([Korolev et al., 2003](#); [Field et al., 2004](#); [Korolev et al., 2017](#)).
122 These findings are very useful constraints of numerical models ([Lohmann and
123 Hoose, 2009](#); [Grabowski et al., 2019](#)). However, in-situ observations of mixed-phase
124 cloud microphysics are technically difficult and sparse in terms of spatial and
125 temporal coverage. Thus, understanding ice formation processes and determining
126 the climatological significance of mixed-phase clouds have proved difficult using
127 existing in-situ observations only.

128

129 Both observations and simulations reveal that ice-nucleating particles (INPs) impact
130 deep convective cloud properties including the persistence of deep convective
131 clouds and precipitation ([Twohy, 2015](#); [Fan et al., 2016](#)). However, the impact of
132 INPs on precipitation from deep convective clouds is still uncertain and may depend
133 on precipitation and cloud types ([van den Heever et al., 2006](#); [Min et al., 2009](#); [Fan
134 et al., 2010](#); [Li and Min, 2010](#)). Although the effects of INPs on convective
135 precipitation are not conclusive, it is certain that the interactions between convective
136 clouds and INPs affect cloud microphysical properties and hence cloud phase
137 distributions. In addition, previous numerical modeling studies on cloud-aerosols
138 interactions have focused on influences of aerosols acting as cloud condensation
139 nuclei (CCN) ([Fan et al., 2016](#)), which are linked to the ice phase e.g. through
140 impacts on the riming efficiency ([Barrett and Hoose, 2023](#)). Given the limited
141 knowledge on ice formation in deep convective clouds and significant uncertainties in
142 ice nucleation parameterizations, it is necessary to conduct sensitivity simulations to
143 investigate how ice formation processes are influenced by INP concentrations and
144 thermodynamic states in deep convective clouds.

145

146 In this study, with the help of realistic convection-permitting simulations using two-
147 moment microphysics, we address how and to what extent INP concentration and
148 thermodynamic state affect the in-cloud and cloud-top phase distributions in deep
149 convective clouds. In particular, cloud properties are retrieved using a satellite
150 forward operator and remote sensing retrieval algorithms with radiative transfer
151 simulations as input for a fair comparison to observations from SEVIRI. This method
152 allows us to compare model simulated cloud properties with remote sensing cloud
153 products directly, and is, to our knowledge, the first time this approach is used for the
154 cloud phase and related microphysical variables. We aim to evaluate the satellite
155 retrieval algorithms and investigate whether passive satellite cloud products can
156 detect cloud microphysical and thermodynamical perturbations.

157

158 This paper is structured as follows: In section 2, we introduce our model setups and
159 the experiment design, the satellite forward operator, remote sensing retrieval
160 algorithms, and datasets. Simulation results for the sensitivity experiments are
161 shown in section 3. Section 4 presents discussions; and we summarize the study
162 and draw conclusions in section 5.

163 **2. Data and Method**

164 **2.1. Model description**

165 The Icosahedral Nonhydrostatic (ICON) model ([Zängl et al., 2015](#)) is a state-of-the-
166 art unified modeling system offering three physics packages, which are dedicated to
167 numerical weather prediction (NWP), climate simulation, and large-eddy simulation.
168 ICON is a fully compressible model and has been developed collaboratively between
169 the German Weather Service (DWD), Max Planck Institute for Meteorology, German
170 Climate Computing Center (DKRZ), and Karlsruhe Institute of Technology (KIT). In
171 order to maximize the model performance and to remove the singularity at the poles,
172 ICON solves the prognostic variables suggested by [Gassmann and Herzog \(2008\)](#),
173 on an unstructured triangular grid with C-type staggering based on a successive
174 refinement of a spherical icosahedron ([Wan et al., 2013](#)). Governing equations are
175 described in [Wan et al. \(2013\)](#) and [Zängl et al. \(2015\)](#). The DWD has operated the
176 ICON model at a spatial resolution of about 13 km on the global scale since January
177 2015. In the global ICON, the higher-resolution ICON-EU (resolution 7 km) nesting

178 area for Europe has been embedded since July 2015. In this study, ICON-2.6.4 with
179 the NWP physics package is used and initial and lateral boundary conditions are
180 provided by the ICON-EU analyses.

181

182 For cloud microphysics, we use an updated version of the two-moment cloud
183 microphysics scheme developed by [Seifert and Beheng \(2006\)](#). The two-moment
184 scheme predicts the number and mass mixing ratios of two liquid (cloud and rain)
185 and four solid (ice, graupel, snow, and hail) hydrometers. The cloud condensation
186 nuclei (CCN) activation is described following the parameterization developed by
187 [Hande et al. \(2016\)](#). Homogeneous freezing, including freezing of liquid water
188 droplets and liquid aerosols, is parametrized according to [Kärcher et al. \(2006\)](#).
189 Heterogeneous ice nucleation, including the immersion and deposition modes, is
190 parameterized as a function of temperature- and ice supersaturation-dependent INP
191 concentration ([Hande et al., 2015](#)). The INP concentration due to immersion
192 nucleation is described as the following equation:

$$193 \quad C_{INP}(T_k) = A \times \exp[-B \times (T_k - T_{min})^C] \quad (1)$$

194 where T_k is the ambient temperature in Kelvin; A , B , and C are fitting constants with
195 different values to represent seasonally varying dust INP concentrations. The
196 parameterization for deposition INPs is simply scaled to the diagnosed relative
197 humidity with respect to ice (RH_{ice}):

$$198 \quad C_{INP}(T_k, RH_{ice}) \approx C_{INP}(T_k) \times DSF(RH_{ice}) \quad (2)$$

$$199 \quad DSF(RH_{ice}) = a \times \arctan(b \times (RH_{ice} - 100) + c) + d \quad (3)$$

200 where $C_{INP}(T_k)$ is given by Equation (1); a , b , c , and d are constants. More details
201 are found in [Hande et al. \(2015\)](#).

202 2.2. Simulation setup and sensitivity experiments

203 In this study, the setup consists of two different domains with one-way nesting
204 covering a major part of central Europe ([Figure 1](#)). The horizontal resolution for the
205 nested domains is halved from 2400 m to 1200 m in the innermost domain, and the
206 time steps for the two domains are 12 s and 6 s, respectively. 150 vertical levels are
207 used, with a grid stretching towards the model top at 21 km. The vertical resolution is
208 the same for all horizontal resolutions and the lowest 1000 m encompass 20 layers.

删除了: Figure 1

设置了格式: 字体: 非倾斜

210 A 1-D vertical turbulence diffusion and transfer scheme is used for the 2400 m and
211 1200 m resolutions, referred to as numerical weather prediction (NWP) physics.
212 Deep convection is assumed to be explicitly resolved, while shallow convection is
213 parameterized for both domains. The simulations are initialized at 00:00 UTC on the
214 study day from ICON-EU analyses and integrated for 24 hours. Simulation results
215 were saved every 15 minutes. At the lateral boundaries of the outer domain, the
216 simulation of the model is updated with 3-hourly ICON-EU analyses. The nested
217 domains are coupled online, and the outer domain provides lateral boundary
218 conditions to the inner domain.

219
220 In nature, INP concentration varies across multiple orders of magnitude ([Hoose and](#)
221 [Möhler, 2012](#); [Kanji et al., 2017](#)). Thus, in our sensitivity experiments, heterogeneous
222 ice formation was scaled by multiplying the default INP concentration (Equation (1))
223 with a factor of 10^{-2} , 10^{-1} , 10^1 , 10^2 , 10^3 for both immersion freezing and deposition ice
224 nucleation. Together with a case with default INP concentration (case CTRL) and
225 one case switching off the secondary-ice production via rime-splintering process (the
226 so called Hallet-Mossop process), 7 cases were created in total to investigate the
227 impact of primary and secondary ice formation on cloud phase distribution in deep
228 convective clouds.

229
230 In order to assess the sensitivity of the cloud phase to thermodynamics, initial and
231 lateral boundary temperature fields are modified with increasing and decreasing
232 temperature increments, named experiments INC and DEC, respectively. The
233 temperature increment is linearly increased/decreased with height from 0 K at 3 km
234 to +/-3K and +/-5K at 12 km, creating 4 sensitivity experiments DEC03, DEC05,
235 INC03, and INC05. Above 12 km, the increment is constant up to the model top.

236 Initial temperature profiles are shown in [Figure 2](#). The increasing or decreasing
237 environmental temperature leads to changes in the lapse rate and the stability of the
238 atmosphere, and hence results in decrease or increase in the convective available
239 potential energy (CAPE), respectively ([Barthlott and Hoose, 2018](#)). Thus, the CAPE
240 increases monotonically from case INC05 (spatial-averaged CAPE at 9:00 UTC: 413
241 J kg^{-1}) to case CTRL (724 J kg^{-1}) and finally to DEC05 (1235 J kg^{-1}). Note that the
242 relative humidity increases/decreases with decreasing/increasing temperature as the
243 specific humidity is unperturbed. The perturbations of INP concentration and

删除了: Figure 2

设置了格式: 字体: 非倾斜

245 initial/lateral temperature profiles are motivated by [Hoose et al. \(2018\)](#) and [Barthlott](#)
246 [and Hoose \(2018\)](#), respectively. Complementary to these earlier studies, we now
247 investigate an ensemble of several deep convective clouds and focus on influences
248 of INP and thermodynamics on cloud phase distribution. Short descriptions of all
249 sensitivity experiments performed in this study are listed in [Table 1](#).

250 2.3. Satellite observations and retrieval algorithms

251 The Spinning Enhanced Visible and Infrared Imager (SEVIRI) is a 12-channel imager
252 on board the geostationary Meteosat Second Generation (MSG) satellites. SEVIRI
253 has one high spatial resolution visible channel (HRV) and 11 spectral channels from
254 0.6 to 14 μm with a 15 min revisit cycle and a spatial resolution of 3 km at nadir
255 ([Schmetz et al., 2002](#)). Based on the spectral measurements of SEVIRI, a cloud
256 property data record, the CLAAS-2 dataset (CLOUD property dAtaset using SEVIRI,
257 Edition 2), has been generated in the framework of the EUMETSAT Satellite
258 Application Facility on Climate Monitoring (CM SAF) ([Benas et al., 2017](#)). CLAAS-2
259 is the successor of CLAAS-1 ([Stengel et al., 2014](#)), for which retrieval updates have
260 been implemented in the algorithm for the detection of clouds compared to CLAAS-1
261 ([Benas et al., 2017](#)) with the temporal coverage being extended to 2004-2015.
262 Retrieval algorithms for parameters that are important for this study are introduced
263 below. Detailed descriptions for the retrieval algorithms are found in [Stengel et al.](#)
264 [\(2014\)](#) and [Benas et al. \(2017\)](#) with the main features being summarized in the
265 following.

266
267 The MSGv2012 software package is employed to detect clouds and their vertical
268 placement ([Derrien and Le Gléau, 2005](#); [Benas et al., 2017](#)). Multi-spectral threshold
269 tests, which depend on illumination and surface types, among other factors, are
270 performed to detect cloud appearances. Each satellite pixel is assigned to categories
271 of cloud-filled, cloud-free, cloud water contaminated, or snow/ice contaminated.
272 Cloud top pressure (CTP) is retrieved with different approaches using input from
273 SEVIRI channels at 6.2, 7.3, 10.8, 12.0, and 13.4 μm ([Menzel et al., 1983](#); [Schmetz](#)
274 [et al., 1993](#); [Stengel et al., 2014](#); [Benas et al., 2017](#)). Cloud top height (CTH) and
275 cloud top temperature (CTT) are derived from CTP using ancillary data for
276 temperature and humidity profiles from ERA-Interim ([Dee et al., 2011](#)). The cloud top

删除了: Table 1

设置了格式: 字体颜色: 自动设置

设置了格式: 字体: 非倾斜, 字体颜色: 自动设置, 检查拼写和语法

278 phase (CPH) retrieval is based on a revised version of the multispectral algorithm
279 developed by [Pavolonis et al. \(2005\)](#). Clouds are categorized initially into six types,
280 that are liquid, supercooled, opaque ice, cirrus, overlap, and overshooting.
281 Subsequently, the binary cloud phase (liquid or ice) is generated based on the six
282 categories ([Benas et al., 2017](#)). Cloud optical and microphysical properties are
283 retrieved using the Cloud Physical Properties (CPP) algorithm ([Roebeling et al.,
284 2006](#)). SEVIRI visible (0.6 μm) and near-infrared (1.6 μm) measurements are used
285 to calculate cloud optical thickness (COT) and cloud particle effective radius (r_e) by
286 applying the [Nakajima and King \(1990\)](#) approach in the CPP algorithm ([Stengel et
287 al., 2014](#); [Benas et al., 2017](#)). Liquid water path (LWP) and ice water path (IWP) are
288 then computed as a function of liquid/ice water density, COT, and r_e of cloud water
289 and cloud ice following the scheme developed by [Stephens \(1978\)](#).

290

291 In this study we used instantaneous CLAAS-2 data with temporal resolution of 15
292 minutes and on native SEVIRI projection and resolution. In addition to the CLAAS-2
293 dataset, the recently developed software suite SEVIRI_ML (Philipp and Stengel
294 (2023) in preparation; code available on Github:
295 https://github.com/danielphilipp/seviri_ml) was applied to the SEVIRI measurements
296 to obtain cloud top phase and cloud top temperature for the selected case.
297 SEVIRI_ML uses a machine learning approach calibrated against Cloud-Aerosol
298 Lidar with Orthogonal Polarization (CALIOP) data. One feature of the SEVIRI_ML is
299 that it also provides pixel-based uncertainties such that values with low reliability can
300 be filtered out. We applied the retrieval algorithms to the model simulations in this
301 study and compared the results to satellite observations. A similar strategy was used
302 by [Kay et al. \(2018\)](#) for the evaluation of precipitation in a climate model with
303 CloudSat observations and termed "scale-aware and definition-aware evaluation".

304 **2.4. Satellite forward operators**

305 In order to compare simulation results and satellite observations directly, SEVIRI-like
306 spectral reflectance and brightness temperatures are calculated using the radiative
307 transfer model for TOVS (RTTOV, v12.3)([Saunders et al., 2018](#)). RTTOV is a fast
308 radiative transfer model for simulating top-of-atmosphere radiances from passive
309 visible, infrared, and microwave downward-viewing satellite radiometers. It has been

310 widely used in simulating synthetic satellite images and assimilating radiances in
311 numerical models ([Saunders et al., 2018](#); [Pscheidt et al., 2019](#); [Senf et al., 2020](#);
312 [Geiss et al., 2021](#); [Rybka et al., 2021](#)).

313

314 In this work, ICON simulated surface skin temperature, near-surface pressure,
315 temperature, specific humidity, wind velocity, total liquid water content, total ice water
316 content, and effective radius of cloud liquid and cloud ice are used as input to drive
317 the RTTOV model. Before inputting to the RTTOV model, ICON simulations are
318 remapped onto SEVIRI's full disc coordinate. Brightness temperatures from 8
319 channels (at 3.9, 6.2, 7.3, 8.7, 9.7, 10.8, 12.0, and 13.4 μm) and reflectance from 3
320 channels (at 0.6, 0.8, and 1.6 μm) simulated by the RTTOV model are used as input
321 to run the remote sensing retrieval algorithms to derive CLAAS-2-like and
322 SEVIRI_ML-like retrievals, named ICON_RTTOV_CLAAS-2 and
323 ICON_RTTOV_SEVIRI_ML products, respectively.

324 **2.5. Synoptic overview**

325 The day 06 June 2016 was selected to analyze, which was dominated by
326 summertime deep convection located in central Europe. The synoptic forcing was
327 weak on the day, and convection was triggered mainly by local thermal instabilities.
328 The day has been discussed frequently in previous studies in terms of convection
329 triggering, cloud microphysics, and its parameterizations ([Keil et al., 2019](#); [Geiss et
330 al., 2021](#)).

331 **3. Results and discussion**

332 Perturbing INP concentration and temperature profiles directly affects microphysical
333 and thermodynamic processes of the developing deep convective clouds, and hence
334 impact in-cloud and cloud-top phase distributions. The following section shows
335 results and discussions on the sensitivities of cloud phase and cloud microphysics to
336 INP concentration and thermodynamic perturbations.

337 **3.1. Spatial distribution of cloud properties**

338 Before analyzing the results of sensitivity experiments, retrieved cloud properties via
339 RTTOV and the CLAAS-2 retrieval scheme for the CTRL case are compared to

340 CLAAS-2 products. Spatial distributions of derived LWP, IWP, and COT at 13:00
341 UTC of the CTRL case and CLAAS-2 satellite observation are shown in [Figure 3](#).
342 Discrepancies are found between ICON simulation and CLAAS-2 satellite
343 observations in terms of spatial coverage and intensity. The ICON simulation
344 overestimates the cloud coverage of low-level liquid clouds compared to CLAAS-2
345 satellite observations, while LWP derived from the ICON simulation (case CTRL) is
346 smaller and more homogeneously distributed than that from the CLAAS-2
347 observation ([Figure 3a](#) and [3b](#)). The spatial distributions of IWP and COT represent
348 the approximate location and spatial extension of deep convective clouds in this
349 study. The ICON simulation could reproduce cores of deep convective clouds of a
350 number and spacing comparable to observations, while the spatial extension and
351 intensity of individual deep convective clouds are not simulated very well by the
352 ICON model. The ICON simulation underestimates the spatial extension of deep
353 convective clouds but overestimates IWP and COT outside the convective cores
354 compared to the CLAAS-2 observation ([Figure 3c-f](#)).

355
356 Overall, the simulated clouds appear to be too homogeneous without sufficient
357 internal structure. [Geiss et al. \(2021\)](#) also reported significant deviations between
358 model simulations and satellite observations. The error sources are manifold and
359 may originate from the model physics as well as from the forward operator and the
360 retrieval algorithm. [Geiss et al. \(2021\)](#) investigated the sensitivity of derived visible
361 and infrared observation equivalents to model physics and operator settings. They
362 found that the uncertainty of the visible forward operator is sufficiently low while
363 infrared channels could bring errors in cloud-top variables. [Geiss et al. \(2021\)](#)
364 concluded that the primary source of deviations is mainly from model physics,
365 especially model assumptions on subgrid-scale clouds. In addition to the subgrid-
366 scale cloud scheme, multiple critical cloud microphysical processes missing from the
367 model, introducing significant uncertainties into the simulation results. For example,
368 entrainment mixing process is not resolved or parameterized in the model, which has
369 essential influences on processes at cloud boundaries and hence the cloud
370 properties ([Mellado, 2017](#)). Moreover, secondary ice processes including droplet
371 shattering and collisional breakup due to ice particles collisions are missing, which
372 have significant impacts on the cloud ice microphysics ([Sullivan et al., 2018](#);
373 [Sotiropoulou et al., 2021](#)).

删除了: Figure 3

删除了: Figure 3

设置了格式: 字体: 非倾斜

删除了: Figure 3

377 **3.2. Sensitivity of microphysical properties to INP perturbation**

378 Perturbing INP concentration results in a direct influence on the heterogeneous
379 freezing processes and hence impacts on cloud microphysical properties.
380 Systematic variations have been found in the spatial- and time-averaged profiles of
381 mass mixing ratios of cloud hydrometeors as shown in [Figure 4](#). All profiles
382 discussed here are averaged over cloudy pixels (defined as having a condensed
383 mass of cloud water plus total cloud ice greater than a threshold of $1.0 \times 10^{-5} \text{ kg kg}^{-1}$)
384 and over the time period from 9:00 to 19:00 UTC, when convection was well
385 developed. The mass concentration of ice crystals decreases with increasing INP
386 concentration ([Figure 4a](#)). However, the mass concentration of snow, graupel, and
387 rainwater increase with increasing INP concentration, especially in the high INP
388 concentration cases (cases $A \times 10^2$ and $A \times 10^3$).

389
390 In order to further reveal why ice crystal mass concentration decreases with
391 increasing INP concentration, we investigate process rates related to ice particle
392 nucleation and growth. [Figure 5](#) shows spatial- and time-averaged (from 9:00 to
393 19:00 UTC) profiles of process rates for homogeneous freezing, heterogeneous
394 freezing, secondary ice production via the rime-splintering process, cloud droplets
395 rimed with ice crystals, rain droplets rimed with ice crystals, and collection between
396 ice and ice crystals. Heterogeneous freezing ([Figure 5a](#)) includes processes of
397 immersion freezing, deposition ice nucleation, and immersion freezing of liquid
398 aerosols ([Kärcher et al., 2006](#); [Hande et al., 2015](#)), see also equations (1) and (2).
399 Process rates of heterogeneous freezing increase significantly with increasing INP
400 concentration compared to the CTRL ([Figure 5a](#)). Compensating the change in
401 heterogeneous freezing, process rates of homogeneous freezing decrease
402 significantly with increasing INP concentration ([Figure 5b](#)). However, a decrease in
403 INP concentration (compared to the CTRL) does not have a strong influence on the
404 heterogeneous freezing mass rate, which is already low compared to the other
405 processes in CTRL. Riming processes of cloud droplets and rain droplets onto ice
406 crystals are greatly invigorated due to enhanced INP concentration ([Figure 5d](#) and
407 [5e](#)). Moreover, process rates of secondary ice production due to rime-splintering are
408 strengthened as well due to the increase in rimed ice, albeit much lower values.
409 [Figure 5f](#) shows process rates of collection between ice and ice crystals. Process

删除了: Figure 4

设置了格式: 字体: 非倾斜

删除了: Figure 4

设置了格式: 字体: 非倾斜

删除了: Figure 5

设置了格式: 字体: 非倾斜

删除了: Figure 5

设置了格式: 字体: 非倾斜

删除了: Figure 5

设置了格式: 字体: 非倾斜

删除了: Figure 5

设置了格式: 字体: 非倾斜

删除了: Figure 5

删除了: Figure 5

418 rates of collection between ice and ice particles increase with increasing INP
419 concentration, especially in high INP concentration cases (cases $A \times 10^2$ and $A \times 10^3$).
420 Process rates of collection of other ice particles all increase with increasing INP
421 concentration, similar to the collection between ice and ice crystals (not shown). The
422 increase in the riming of clouds and rain droplets onto ice crystals and collections
423 between ice particles leads to the increase in the mass concentration of snow,
424 graupel, and hail (Figure 4b and 4c). However, the total mass increase in snow,
425 graupel, and hail do not outbalance the decrease in the mass concentration of ice
426 crystals (Figure 4). The weakened homogeneous freezing is most likely the dominant
427 factor leading to the decrease in ice mass concentration in high INP cases,
428 considering the magnitude of the process rate of homogeneous freezing (Figure 5b).
429 Supercooled liquid and cloud droplets have been converted into ice crystals before
430 reaching the homogeneous freezing layer, leading to fewer supercooled droplets
431 remaining for homogeneous freezing. Even though homogeneous freezing is
432 weakened in high INP cases, the process rate of homogeneous freezing is still larger
433 than heterogeneous freezing, which means homogeneous freezing is the dominant
434 ice formation process in the convective clouds discussed in this study. Moreover, the
435 enhanced production of large ice particles (snow, graupel, and hail) in the highest
436 INP case, which sediment more rapidly to lower levels, leads to increased surface
437 precipitation by about 10% in the $A \times 10^3$ case (not shown). Interestingly, ice crystal
438 effective radius (r_e^{ice}) increases monotonically with increasing INP concentration,
439 especially in the mixed-phase layer (Figure 4e). Zhao et al. (2019) also reported an
440 increased r_e^{ice} with polluted continental aerosols in their simulated moderate
441 convection cases, and they attributed it to enhanced heterogeneous freezing and
442 prolonged ice crystal growth at higher INP loading.

443
444 This competition between homogeneous and heterogeneous freezing has been
445 discussed in previous studies (Heymsfield et al., 2005; Deng et al., 2018; Takeishi
446 and Storelvmo, 2018). In contrast, simulations of mixed-phase moderately deep
447 convective clouds by Miltenberger and Field (2021) indicate that cloud ice mass
448 concentration increases with increasing INP concentration, which is in opposition to
449 the findings in this work. The main reason is that the CTT is about -18°C in
450 Miltenberger and Field (2021)'s study, and heterogeneous freezing does not

删除了: Figure 4

设置了格式: 字体: 非倾斜

删除了: Figure 4

设置了格式: 字体: 非倾斜

删除了: Figure 5

设置了格式: 字体: 非倾斜

删除了: Figure 4

455 compete with homogeneous freezing. Thus, results on INPs effects on glaciation
456 processes in convective clouds can be opposite under different conditions.

457 3.3. Cloud liquid mass fraction

458 Varying the INP concentration has a direct impact on the primary ice formation.
459 Thus, it affects cloud liquid mass fraction within the clouds (directly for all cloudy
460 layers where heterogeneous freezing is active and indirectly for warmer and colder
461 temperatures) and at the cloud top. Cloud liquid mass fraction is defined as the ratio
462 of mass mixing ratio between cloud droplets (q_c) and the sum of cloud droplets and
463 cloud ice crystals (q_i). In-cloud liquid mass fraction, sampled at a time interval of 15
464 minutes between 9:00 to 19:00 from all cloudy pixels, is shown as scatterplots
465 versus temperature in [Figure 6a-d](#). The corresponding frequencies of the occurrence
466 of the temperature/liquid fraction bins are shown in [Figure 6e-h](#). Similar analyses
467 were made by [Hoose et al. \(2018\)](#), but for idealized simulations of deep convective
468 clouds. In-cloud liquid mass fractions smaller than 0.5 are quite common already at
469 temperature just below $-3\text{ }^\circ\text{C}$ except for the case without rime-splintering process
470 ($A \times 10^0$ _NSIP). The decrease in INP concentrations has limited effects on the in-
471 cloud liquid mass fraction ([Figure 6c](#) and [6g](#)), while a stronger influence has been
472 found in the case with enhanced INP concentration ([Figure 6d](#) and [6h](#)). The number
473 of pixels having high liquid mass fraction values at temperatures lower than $-30\text{ }^\circ\text{C}$
474 decreases with increasing INP concentration. In addition, more and more pixels
475 having liquid mass fraction smaller than 0.5 appear with increasing INP
476 concentration and the number of pure ice pixels increases with increasing INP
477 concentration as well. This is because higher INP concentration intensifies the
478 heterogeneous freezing processes (immersion freezing and deposition ice
479 nucleation) and invigorates the rime-splintering process as well (will be discussed in
480 section 3.4). Interestingly, at the lower end of the mixed-phase temperature range ($-$
481 $38\text{ }^\circ\text{C}$ \sim $-28\text{ }^\circ\text{C}$), there are fewer pixels having high liquid mass fraction in the high INP
482 case, and those remaining are mainly the ones at high vertical velocities (above ~ 10
483 m/s). This is probably because supercooled droplets are more easily frozen in high
484 INP cases and stronger updrafts are needed to offset the Wegener-Begeron-
485 Findeisen ([WBF](#)) process to maintain the supersaturation with respect to water.
486 Switching off the secondary ice production via rime-splintering process, pixels having

删除了: Figure 6

设置了格式: 字体: 非倾斜

删除了: Figure 6

设置了格式: 字体: 非倾斜

删除了: Figure 6

设置了格式: 字体: 非倾斜

删除了: Figure 6

设置了格式: 字体: 非倾斜

491 a liquid mass fraction smaller than 0.9 are reduced significantly at temperatures
492 between -10 °C and 0 °C (Figure 6b and 6f).

删除了：Figure 6

设置了格式：字体：非倾斜

493
494 At the cloud top (Figure 7), the number of pixels having a liquid mass fraction smaller
495 than 0.5 increases with increasing INP concentration, which is the same as within
496 the clouds. “Cloud top” is defined as the height of the uppermost cloud layer (which
497 has a condensed mass of cloud water plus cloud total cloud ice greater than a
498 threshold of 1.0×10^{-5} kg kg⁻¹) in a pixel column. At the cloud top, the liquid mass
499 fraction has a more polarized distribution, with either large values or small values,
500 and intermediate values are less common than within the clouds. This is because the
501 vertical velocities at the cloud top are significantly smaller compared to that within
502 the cloud, which leads to a more efficient WBF process at the cloud top.

删除了：Figure 7

设置了格式：字体：非倾斜

删除了：egener-Begeron-Findeisen

503 3.4. Liquid cloud pixel fraction

504 Liquid cloud pixel fractions are calculated differently for model simulations and
505 retrieved cloud products. For simulation results, a cloudy pixel having a cloud liquid
506 mass fraction larger than 0.5 is counted as a liquid pixel, otherwise, it is an ice pixel.
507 Both CLAAS-2 and SEVIRI_ML products and the corresponding retrievals derived
508 from ICON simulations by the satellite forward operators (see section 2.4) provide
509 binary cloud phase information (liquid or ice) only. For these data, the liquid cloud
510 pixel fraction is calculated as the ratio between the number of liquid cloud pixels and
511 the sum of all cloudy pixels.

512
513 Liquid cloud pixel fractions within clouds and at the cloud top are shown in Figure 8.
514 Decrease in INP concentration has limited impacts on the liquid cloud pixel fraction
515 for in-cloud layers. Increase in INP concentration leads to a decrease in liquid cloud
516 pixel fraction but not monotonically (Figure 8a). The decrease in liquid cloud pixel
517 fraction is significant in the highest INP concentration case (case $A \times 10^3$), while
518 decreases in intermediate INP concentration cases (cases $A \times 10^1$ and $A \times 10^2$) are
519 only obvious in temperature ranges from -30 °C to -20 °C and from -15 °C to -5 °C.
520 Moreover, liquid mass fraction decreases monotonically with increasing INP
521 concentration in the temperature range from about -15 to -35 °C both within the cloud
522 and at the cloud top (except for the lowest INP concentrations), and the decreasing

删除了：Figure 8

设置了格式：字体：非倾斜

删除了：Figure 8

设置了格式：字体：非倾斜

528 trend is more significant at the cloud top compared to within the cloud (not shown).
529 Switching off the rime-splintering process results in an increase in liquid cloud pixel
530 fraction in the temperature range between -10 °C and -3 °C, which is consistent with
531 the strong decrease in pixels of cloud liquid mass fraction lower than 0.9 in the same
532 temperature range (Figure 7b). The temperature at which the liquid cloud pixel
533 fraction equals 0.5 is often termed “glaciation temperature”. The glaciation
534 temperature shifts slightly to a warmer temperature by ~2 °C at the highest INP
535 concentration case (case A×10³, Figure 8a).

删除了: Figure 7

设置了格式: 字体: 非倾斜

删除了: Figure 8

537 Sensitivities of the cloud phase to INP concentration are more complex at the cloud
538 top than inside the cloud. Liquid cloud pixel fractions at the cloud top calculated
539 directly from ICON simulations on its native grid (~1200 m) are shown in Figure 8b.

删除了: Figure 8

设置了格式: 字体: 非倾斜

540 Cloud-top liquid pixel fraction decreases significantly with increasing INP
541 concentration. In the temperature range between -35 °C and -15 °C, where
542 heterogeneous freezing processes (immersion freezing and deposition nucleation)
543 are dominant, the impact of INP is most pronounced. Above -15 °C, the impact of
544 INP does not disappear, especially in the highest INP concentration case (case
545 A×10³). This is mostly likely due to the sedimentation of ice crystals from upper
546 layers and the secondary ice production invigorated by the WBF process. Switching
547 off the rime-splintering process increases cloud-top liquid pixel fraction only slightly
548 in the temperature range from -10 °C to -3 °C and is almost identical to the control
549 run (case CTRL) outside this temperature range. Interestingly, the shift of glaciation
550 temperature with increasing INP concentration is about 8 °C (Figure 8b) at the cloud
551 top, which is stronger than that inside the clouds (~2 °C, Figure 8a). A possible
552 explanation is that, typically, the vertical velocity at the cloud top is smaller than
553 within the cloud and the ice formation through the WBF process is expected to be
554 more efficient. Thus, the WBF process is more sensitive to INP perturbation at the
555 cloud top than within clouds, and leads to the glaciation temperature shifting to be
556 more significant at the cloud top.

删除了: egener-Begeron-Findeisen

删除了: Figure 8

设置了格式: 字体: 非倾斜

删除了: Figure 8

设置了格式: 字体: 非倾斜

删除了: egener-Bergeron-Findeisen

删除了: egener-Begeron-Findeisen

557
558 Liquid cloud pixel fractions at the cloud top calculated directly from ICON simulations
559 on SEVIRI's grid (~ 5000 m) are shown in Figure 8c. They are noisier and do not
560 exhibit the small minimum between -10 °C and -3 °C related to rime-splintering, but

删除了: Figure 8

设置了格式: 字体: 非倾斜

570 are otherwise very similar to [Figure 8b](#). In contrast, the scale-aware and definition-
571 aware ICON_RTTOV_CLAAS-2 cloud-top liquid pixel fractions shown in [Figure 8d](#)
572 differ markedly from the direct or regridded model output. Above -23 °C, increase
573 and decrease in INP concentration both lead to a decrease in cloud-top liquid pixel
574 fraction at certain temperature, but the high INP concentration cases (cases $A \times 10^2$
575 and $A \times 10^3$), still exhibit the lowest liquid fractions, and case $A \times 10^0$ _NSIP the highest.
576 Thus, the fingerprints of primary and secondary ice formation are retained in the
577 ICON_RTTOV_CLAAS-2 liquid fraction in this temperature range only for very strong
578 perturbations. At the same time, it must be noted that the decrease of the liquid pixel
579 fraction to values around 0.8 above -15 °C is not related to the rime-splintering
580 process, but to the application of the CLAAS-2 satellite simulator. Below -23 °C, in
581 the high INP cases $A \times 10^2$ and $A \times 10^3$, cloud-top liquid pixel fractions even increase
582 with increasing INP concentration. In moderate and low INP cases, the impacts of
583 INP perturbation are not pronounced. Moreover, the shape of cloud-top liquid pixel
584 fraction decreasing with cloud-top temperature is different from that in [Figure 8b](#).
585 Here, the fingerprints of the ice formation processes are completely lost. As
586 demonstrated in [Figure 8c](#), remapping of simulation data onto SEVIRI's coarser grid
587 is not the cause of liquid pixel fraction difference between direct ICON output and the
588 ICON_RTTOV_CLAAS-2 diagnostics, but the CLAAS-2 retrieval algorithm itself is
589 responsible.

590

591 The satellite observed cloud-top liquid pixel fraction from CLAAS-2 is plotted as a
592 grey dashed line in [Figure 8d](#). It does not reach 1.0 for all cases even as the cloud-
593 top temperature is approaching 0 °C, and shows a different temperature dependency
594 than the simulated curves. No matter how strong the INP concentration and rime-
595 splintering are perturbed, the retrieved cloud-top liquid pixel fractions from simulation
596 data deviate strongly from the CLAAS-2 products. In this context one should note
597 that in particular cloud edges have been found to be problematic situations for the
598 cloud retrievals, being to some extent responsible for biasing the liquid-pixel fraction
599 towards smaller values, in particular for the CLAAS-2 data.

600

601 Finally, the comparison to observations is repeated with the SEVIRI_ML retrieval
602 scheme applied to both simulated radiances (ICON_RTTOV_SEVIRI_ML) and the

删除了: Figure 8
设置了格式: 字体: 非倾斜
删除了: Figure 8
设置了格式: 字体: 非倾斜

删除了: Figure 8
设置了格式: 字体: 非倾斜
删除了: Figure 8
设置了格式: 字体: 非倾斜

删除了: Figure 8
设置了格式: 字体: 非倾斜

608 SEVIRI observations themselves (Figure 8e). As SEVIRI_ML provides uncertainty
609 estimates, pixels for which either the cloud mask uncertainty or the cloud phase
610 uncertainty is larger than 10% are filtered out. While this ensures that only very
611 certain values are kept, it has a significant impact on the number of remaining values
612 as more than 90% of the pixels are filtered out. The filtering affects pixels rather
613 randomly, thus we could not identify any patterns of pixels, such as cloud edges, that
614 are primarily affected by the filtering. The resulting liquid pixel fractions
615 ICON_RTTOV_SEVIRI_ML bear a much stronger similarity to the regrided model
616 output in Figure 8c. Remaining differences are a noisier behavior, a plateau of non-
617 zero liquid pixel fractions even below -40 °C, and a general shift to lower
618 temperatures. SEVIRI_ML applied to observations (dashed black line in Figure 8e),
619 with the same uncertainty criterion, exhibits the expected behavior with a liquid
620 fraction of approximately 1 above -10 °C and 0 below approximately -30 °C, and
621 results in a very good agreement to the $A \times 10^3$ case. Generally, the SEVIRI_ML
622 retrieval algorithm is assumed to perform better than the CLAAS-2 scheme for both
623 cloud top temperature and cloud phase. This is because SEVIRI_ML employs state-
624 of-the-art neural networks to emulate CALIOP v4 data. Moreover, SEVIRI_ML
625 provides uncertainty estimates which facilitates flitting out pixels with high
626 uncertainties. Nevertheless, retrieval inaccuracies are unavoidable for passive
627 satellite retrievals which holds true for CLAAS-2 but also for SEVIRI_ML.

删除了: Figure 8

设置了格式: 字体: 非倾斜

删除了: Figure 8

设置了格式: 字体: 非倾斜

删除了: Figure 8

设置了格式: 字体: 非倾斜

628 3.5. Sensitivity of cloud phase to atmospheric stability perturbations

629 In addition to the reference run (case CTRL), four cases with perturbations in initial
630 temperatures are analyzed. Mean updraft velocities increase gradually from the low
631 CAPE case INC05 to high CAPE case DEC05 (Figure 9) and cause differences in
632 cloud microphysics and cloud phase distributions.

删除了: Figure 9

设置了格式: 字体: 非倾斜

634 In-cloud and cloud-top liquid cloud pixel fractions for the five cases are shown in
635 Figure 10. Systematic shifting of liquid cloud pixel fractions is detected both inside
636 clouds and at the cloud top. Liquid cloud pixel fraction decreases with increasing
637 CAPE from INC05 to DEC05. Both in-cloud and cloud-top glaciation temperatures
638 shift toward warmer temperatures as the CAPE increases from case INC05 to
639 DEC05. This is different from the results reported by Hoose et al. (2018) that cloud-

删除了: Figure 10

设置了格式: 字体: 非倾斜

645 top glaciation temperatures hardly changed with increasing temperature in the
646 boundary-layer by 2 °C, and appears to be contradictory to the expectation that
647 stronger vertical velocities result in a lower glaciation temperature due to
648 suppression of the W_{BF} process (Korolev, 2007). Further analysis (not shown)
649 revealed that the mass concentration of cloud ice particle increases while the mass
650 concentration of cloud droplet decreases with the increase in CAPE from case
651 INC05 to DEC05. Moreover, homogeneous and heterogeneous freezing are both
652 enhanced in the high CAPE cases (Figure 11), possibly due to more transport of
653 moisture to upper levels in the stronger updrafts (Figure 9). With more ice generated,
654 the W_{BF} process can be stimulated despite the higher updrafts. Interestingly, cloud-
655 top liquid pixel fractions from the two high CAPE cases (cases DEC03 and DEC05)
656 are closer to SEVIRI observations, both using the CLAAS-2 retrieval (Figure 10c)
657 and the SEVIRI_ML retrieval (Figure 10d), especially in the temperature range
658 between -10 and -28 °C.

659 Compared to the INP perturbation, the impact of thermodynamical perturbation on
660 cloud phase distribution is significantly stronger within the cloud (Figure 8a and
661 Figure 10a). At the cloud top, the effect of perturbation in thermodynamics on the
662 cloud phase distribution is as large as the largest INP perturbation (case A×10³).
663 Moreover, the impacts of thermodynamical perturbation on domain-averaged profiles
664 of cloud hydrometeors and process rates related to the ice cloud process are also
665 significantly stronger than the INP perturbation. Thus, the thermodynamical
666 perturbation is stronger than the INP perturbation when the entire depth of the cloud
667 is considered. Overall, perturbing initial thermodynamic states or CAPE of convective
668 clouds is as important as and may even stronger than the modifications to cloud
669 heterogeneous freezing parameterizations.
670

671 4. Conclusions

672 Remote sensing products, which cover the entire globe, provide a unique opportunity
673 to constrain the representation of cloud microphysics in global and regional
674 numerical models. In this study, instead of comparing simulation results to satellite
675 observations directly, we derived cloud properties using a radiative transfer model
676 and two different satellite remote sensing retrieval algorithms and then performed the

删除了: egener-Bergeron-Findeisen

删除了: Figure 11

删除了: Figure 9

删除了: egener-Begeron-Findeisen

删除了: Figure 10

设置了格式: 字体: 非倾斜

删除了: Figure 10

设置了格式: 字体: 非倾斜

683 comparison. This enables us to make apples-to-apples comparisons between model
684 simulations and satellite observations. A series of numerical experiments were
685 performed applying convection-permitting simulations with perturbations in INP
686 concentrations and initial thermodynamic states to investigate their impacts on cloud
687 phase distributions in deep convective clouds. Moreover, cloud properties were
688 derived using a satellite forward operator and retrieval algorithms with ICON
689 simulations as input, and compared with CLAAS-2 and SEVIRI_ML satellite cloud
690 products to evaluate whether satellite retrievals could detect perturbations in cloud
691 microphysics and thermodynamics. Uncertainties in the forward operator were
692 however not assessed in this study, which may influence the validity of
693 corresponding results in some extent.

694

695 INP concentration was found to have a significant role in shaping cloud phase
696 distributions both within clouds and at the cloud top. Cloud liquid pixel fraction
697 decreased with increasing INP concentration both within the cloud and at the cloud
698 top, indicating a higher glaciation temperature and more intense heterogeneous
699 freezing processes in enhanced INP concentration cases. Interestingly, the
700 influences of INP did not increase linearly but are more pronounced in the high INP
701 concentration cases. In addition, the shifting of glaciation temperature was more
702 significant at the cloud top than within the cloud, which means the impact of INP
703 concentration on cloud phase distribution is more pronounced at the cloud top. It
704 turned out that with the CLAAS-2 retrieval scheme, the INP sensitivity of the cloud-
705 top phase distribution was not detectable, while the SEVIRI_ML retrieval scheme, for
706 which the most uncertain pixels could be excluded, resulted in a better agreement
707 and retained the sensitivity to INP. In contrast, secondary ice production via rime-
708 splintering did not have a detectable impact on the cloud-top phase distribution.
709 Therefore, in future studies, we recommend using the SEVIRI_ML retrieval scheme
710 and SEVIRI_ML satellite-based cloud products.

711

712 Ice crystal mass concentration did not increase but decreases with increasing INP
713 concentrations in the simulated deep convective clouds. Process rate analyses
714 revealed that heterogeneous freezing process rates increased with increasing INP
715 concentration, while homogeneous freezing process rates decreased with increasing
716 INP concentration. The competition between heterogeneous freezing and

717 homogeneous freezing for water vapor suppressed ice formation via homogeneous
718 freezing, which was the dominant nucleation process in the simulated deep
719 convective clouds, and hence reduced the cloud ice mass concentration. The
720 increase in heterogeneous nucleation in high INP cases invigorated riming and
721 collection processes of ice particles, making it easier for small ice crystals to grow
722 into large ice aggregates and sediment to lower levels. This was the reason why
723 precipitation increases in enhanced INP cases.

724

725 Perturbations in initial thermodynamic states had a strong impact on the cloud phase
726 distribution both within the cloud and at the cloud top, although the used
727 perturbations might be rather large compared to initial condition uncertainty in a
728 weather forecasting context. Moreover, cloud thermodynamics can perturb the cloud
729 phase distribution even stronger than microphysics. To completely distinguish
730 microphysical impacts from thermodynamic impacts, applying a piggybacking
731 approach ([Grabowski, 2015](#); [Thomas et al., 2023](#)) in future simulations is necessary.

732

733 Utilizing satellite forward operator (the RTTOV radiative model) and remote sensing
734 retrieval algorithms enabled us to derive cloud-top microphysical properties and
735 compare simulation results to satellite products more consistently. However, there
736 were significant differences in retrieved cloud-top liquid fractions between model
737 simulations and satellite products. The sources of errors were very complicated and
738 may come from simulation results, satellite operators, and retrieval algorithms, which
739 will be investigated in the future. Moreover, the cloud-top property analysis
740 presented in this study was based on domain-wide statistics, including clouds of
741 varying types. Statistical results could differ if individual clouds are tracked, as clouds
742 differ in different experiments in terms of locations and extensions. Although there
743 are significant uncertainties in satellite forward operators and retrieval algorithms,
744 passively remote-sensed cloud products provide potential opportunities to constrain
745 microphysical processes in numerical models.

746

747 Simulation results of this study revealed a close dependence of heterogeneous
748 freezing and cloud phase distribution on INP concentrations. Despite this finding, the
749 ice formation processes in deep convective clouds remain poorly understood. It is
750 necessary to investigate how and in which conditions the competition of

751 heterogeneous with homogeneous freezing for water vapor and cloud water depends
752 on INP availability and vertical velocities in different types of deep convective clouds.
753 Moreover, the importance of other secondary ice production processes than rime-
754 splintering (droplet shattering and collisional breakup) in deep convective clouds
755 need to be quantified in the future.
756

757 **Competing interests**

758 One of the (co-)authors (Corinna Hoose) is a member of the editorial board of
759 Atmospheric Chemistry and Physics.
760

761 **Acknowledgments**

762 This project has received funding from the European Research Council (ERC) under
763 the European Union's Horizon 2020 research and innovation programme under grant
764 agreement 714062 (ERC Starting Grant "C2Phase"). We gratefully acknowledge the
765 computing time allowed by the German Climate Computing Centre (DKRZ) on the
766 HPC system Mistral and the Steinbuch Centre for Computing (SCC) on the HPC
767 system ForHLR II. The contribution of Martin Stengel was supported by EUMETSAT
768 and its member states through CM SAF.
769

770 **References**

- 771 Barrett, A. I. and Hoose, C.: Microphysical pathways active within thunderstorms and
772 their sensitivity to CCN concentration and wind shear, *Journal of Geophysical*
773 *Research: Atmospheres*, 128, e2022JD036965,
774 <https://doi.org/10.1029/2022JD036965>, 2023.
- 775 Barthlott, C. and Hoose, C.: Aerosol effects on clouds and precipitation over central
776 Europe in different weather regimes, *Journal of the Atmospheric Sciences*, 75,
777 4247-4264, <https://doi.org/10.1175/JAS-D-18-0110.1>, 2018.
- 778 Benas, N., Finkensieper, S., Stengel, M., van Zadelhoff, G. J., Hanschmann, T.,
779 Hollmann, R., and Meirink, J. F.: The MSG-SEVIRI-based cloud property data
780 record CLAAS-2, *Earth Syst. Sci. Data*, 9, 415-434,
781 <http://dx.doi.org/10.5194/essd-9-415-2017>, 2017.
- 782 Bruno, O., Hoose, C., Storelvmo, T., Coopman, Q., and Stengel, M.: Exploring the
783 cloud top phase partitioning in different cloud types using active and passive

784 satellite sensors, *Geophysical Research Letters*, 48, e2020GL089863-
785 e082020GL089863, <https://doi.org/10.1029/2020GL089863>, 2021.

786 Coopman, Q., Hoose, C., and Stengel, M.: Analysis of the thermodynamic phase
787 transition of tracked convective clouds based on geostationary satellite
788 observations, *Journal of Geophysical Research: Atmospheres*, 125,
789 e2019JD032146, <https://doi.org/10.1029/2019JD032146>, 2020.

790 Coopman, Q., Hoose, C., and Stengel, M.: Analyzing the thermodynamic phase
791 partitioning of mixed phase clouds over the southern ocean using passive
792 satellite observations, *Geophysical Research Letters*, 48, e2021GL093225,
793 <https://doi.org/10.1029/2021GL093225>, 2021.

794 Dee, D. P., Uppala, S. M., Simmons, A. J., Berrisford, P., Poli, P., Kobayashi, S.,
795 Andrae, U., Balmaseda, M. A., Balsamo, G., Bauer, P., Bechtold, P., Beljaars,
796 A. C. M., van de Berg, L., Bidlot, J., Bormann, N., Delsol, C., Dragani, R.,
797 Fuentes, M., Geer, A. J., Haimberger, L., Healy, S. B., Hersbach, H., Hólm, E.
798 V., Isaksen, I., Kållberg, P., Köhler, M., Matricardi, M., McNally, A. P., Monge-
799 Sanz, B. M., Morcrette, J. J., Park, B. K., Peubey, C., de Rosnay, P.,
800 Tavolato, C., Thépaut, J. N., and Vitart, F.: The ERA-Interim reanalysis:
801 configuration and performance of the data assimilation system, *Quarterly*
802 *Journal of the Royal Meteorological Society*, 137, 553-597,
803 <https://doi.org/10.1002/qj.828>, 2011.

804 Deng, X., Xue, H., and Meng, Z.: The effect of ice nuclei on a deep convective cloud
805 in South China, *Atmospheric Research*, 206, 1-12,
806 <https://doi.org/10.1016/j.atmosres.2018.02.013>, 2018.

807 Derrien, M. and Le Gléau, H.: MSG/SEVIRI cloud mask and type from SAFNWC,
808 *International Journal of Remote Sensing*, 26, 4707-4732,
809 <https://doi.org/10.1080/01431160500166128>, 2005.

810 Fan, J., Comstock, J. M., and Ovchinnikov, M.: The cloud condensation nuclei and
811 ice nuclei effects on tropical anvil characteristics and water vapor of the
812 tropical tropopause layer, *Environmental Research Letters*, 5, 044005,
813 <https://doi.org/10.1088/1748-9326/5/4/044005>, 2010.

814 Fan, J., Wang, Y., Rosenfeld, D., and Liu, X.: Review of aerosol–cloud interactions:
815 Mechanisms, significance, and challenges, *Journal of the Atmospheric*
816 *Sciences*, 73, 4221-4252, <https://doi.org/10.1175/JAS-D-16-0037.1>, 2016.

817 Field, P. R., Hogan, R. J., Brown, P. R. A., Illingworth, A. J., Choulaton, T. W., Kaye,
818 P. H., Hirst, E., and Greenaway, R.: Simultaneous radar and aircraft
819 observations of mixed-phase cloud at the 100 m scale, *Quarterly Journal of*
820 *the Royal Meteorological Society*, 130, 1877-1904,
821 <https://doi.org/10.1256/qj.03.102>, 2004.

822 Gassmann, A. and Herzog, H.-J.: Towards a consistent numerical compressible non-
823 hydrostatic model using generalized Hamiltonian tools, *Quarterly Journal of*
824 *the Royal Meteorological Society*, 134, 1597-1613,
825 <http://dx.doi.org/10.1002/qj.297>, 2008.

826 Geiss, S., Scheck, L., de Lozar, A., and Weissmann, M.: Understanding the model
827 representation of clouds based on visible and infrared satellite observations,
828 *Atmos. Chem. Phys.*, 21, 12273-12290, [https://doi.org/10.5194/acp-21-12273-](https://doi.org/10.5194/acp-21-12273-2021)
829 [2021](https://doi.org/10.5194/acp-21-12273-2021), 2021.

830 Grabowski, W. W.: Untangling microphysical impacts on deep convection applying a
831 novel modeling methodology, *Journal of the Atmospheric Sciences*, 72, 2446-
832 2464, <https://doi.org/10.1175/JAS-D-14-0307.1>, 2015.

833 Grabowski, W. W., Morrison, H., Shima, S.-I., Abade, G. C., Dziekan, P., and
834 Pawlowska, H.: Modeling of cloud microphysics: Can we do better?, *Bulletin*
835 *of the American Meteorological Society*, 100, 655-672,
836 <https://doi.org/10.1175/BAMS-D-18-0005.1>, 2019.

837 Hande, L. B., Engler, C., Hoose, C., and Tegen, I.: Seasonal variability of Saharan
838 desert dust and ice nucleating particles over Europe, *Atmos. Chem. Phys.*,
839 15, 4389-4397, <http://dx.doi.org/10.5194/acp-15-4389-2015>, 2015.

840 Hande, L. B., Engler, C., Hoose, C., and Tegen, I.: Parameterizing cloud
841 condensation nuclei concentrations during HOPE, *Atmos. Chem. Phys.*, 16,
842 12059-12079, <http://dx.doi.org/10.5194/acp-16-12059-2016>, 2016.

843 Hawker, R. E., Miltenberger, A. K., Wilkinson, J. M., Hill, A. A., Shipway, B. J., Cui,
844 Z., Cotton, R. J., Carslaw, K. S., Field, P. R., and Murray, B. J.: The
845 temperature dependence of ice-nucleating particle concentrations affects the
846 radiative properties of tropical convective cloud systems, *Atmos. Chem.*
847 *Phys.*, 21, 5439-5461, <https://doi.org/10.5194/acp-21-5439-2021>, 2021.

848 Heymsfield, A. J., Miloshevich, L. M., Schmitt, C., Bansemer, A., Twohy, C., Poellot,
849 M. R., Fridlind, A., and Gerber, H.: Homogeneous ice nucleation in subtropical
850 and tropical convection and its influence on cirrus anvil microphysics, *Journal*
851 *of the Atmospheric Sciences*, 62, 41-64, <http://dx.doi.org/10.1175/JAS-3360.1>,
852 2005.

853 Hoose, C. and Möhler, O.: Heterogeneous ice nucleation on atmospheric aerosols: a
854 review of results from laboratory experiments, *Atmos. Chem. Phys.*, 12, 9817-
855 9854, <https://doi.org/10.5194/acp-12-9817-2012>, 2012.

856 Hoose, C., Kärner, M., and Barthlott, C.: Cloud top phase distributions of simulated
857 deep convective clouds, *Journal of Geophysical Research: Atmospheres*,
858 123, 10,410-464,476, <https://doi.org/10.1029/2018JD028381>, 2018.

859 Kanji, Z. A., Ladino, L. A., Wex, H., Boose, Y., Burkert-Kohn, M., Cziczo, D. J., and
860 Krämer, M.: Overview of ice nucleating particles, *Meteorological Monographs*,
861 58, 1.1-1.33, <https://doi.org/10.1175/AMSMONOGRAPHS-D-16-0006.1>, 2017.

862 Kärcher, B., Hendricks, J., and Lohmann, U.: Physically based parameterization of
863 cirrus cloud formation for use in global atmospheric models, *Journal of*
864 *Geophysical Research: Atmospheres*, 111,
865 <https://doi.org/10.1029/2005JD006219>, 2006.

866 Kay, J. E., L'Ecuyer, T., Pendergrass, A., Chepfer, H., Guzman, R., and Yettella, V.:
867 Scale-aware and definition-aware evaluation of modeled near-surface
868 precipitation frequency using CloudSat observations, *Journal of Geophysical*
869 *Research: Atmospheres*, 123, 4294-4309,
870 <https://doi.org/10.1002/2017JD028213>, 2018.

871 Keil, C., Baur, F., Bachmann, K., Rasp, S., Schneider, L., and Barthlott, C.: Relative
872 contribution of soil moisture, boundary-layer and microphysical perturbations
873 on convective predictability in different weather regimes, *Quarterly Journal of*
874 *the Royal Meteorological Society*, 145, 3102-3115,
875 <https://doi.org/10.1002/qj.3607>, 2019.

876 Korolev, A. and Isaac, G. A.: Relative humidity in liquid, mixed-phase, and ice
877 clouds, *Journal of the Atmospheric Sciences*, 63, 2865-2880,
878 <https://doi.org/10.1175/JAS3784.1>, 2006.

879 Korolev, A.: Limitations of the Wegener–Bergeron–Findeisen mechanism in the
880 evolution of mixed-phase clouds, *Journal of the Atmospheric Sciences*, 64,
881 3372-3375, <http://dx.doi.org/10.1175/JAS4035.1>, 2007.

882 Korolev, A., McFarquhar, G., Field, P. R., Franklin, C., Lawson, P., Wang, Z.,
883 Williams, E., Abel, S. J., Axisa, D., Borrmann, S., Crosier, J., Fugal, J.,
884 Krämer, M., Lohmann, U., Schlenker, O., Schnaiter, M., and Wendisch, M.:
885 Mixed-phase clouds: Progress and challenges, *Meteorological Monographs*,
886 58, 5.1-5.50, <https://doi.org/10.1175/AMSMONOGRAPHS-D-17-0001.1>, 2017.

887 Korolev, A. V., Isaac, G. A., Cober, S. G., Strapp, J. W., and Hallett, J.:
888 Microphysical characterization of mixed-phase clouds, *Quarterly Journal of*
889 *the Royal Meteorological Society*, 129, 39-65,
890 <https://doi.org/10.1256/qj.01.204>, 2003.

891 Li, R. and Min, Q. L.: Impacts of mineral dust on the vertical structure of precipitation,
892 *Journal of Geophysical Research: Atmospheres*, 115,
893 <https://doi.org/10.1029/2009JD011925>, 2010.

894 Li, X., Tao, W.-K., Masunaga, H., Masunaga, Gu, G., and Zeng, X.: Aerosol effects
895 on cumulus congestus population over the tropical Pacific: A cloud-resolving
896 modeling study, *Journal of the Meteorological Society of Japan*, 91, 817-833,
897 10.2151/jmsj.2013-607, 2013.

898 Lohmann, U. and Hoose, C.: Sensitivity studies of different aerosol indirect effects in
899 mixed-phase clouds, *Atmos. Chem. Phys.*, 9, 8917-8934,
900 <https://doi.org/10.5194/acp-9-8917-2009>, 2009.

901 Matus, A. V. and L'Ecuyer, T. S.: The role of cloud phase in Earth's radiation budget,
902 *Journal of Geophysical Research: Atmospheres*, 122, 2559-2578,
903 <https://doi.org/10.1002/2016JD025951>, 2017.

904 McCoy, D. T., Tan, I., Hartmann, D. L., Zelinka, M. D., and Storelvmo, T.: On the
905 relationships among cloud cover, mixed-phase partitioning, and planetary
906 albedo in GCMs, *Journal of Advances in Modeling Earth Systems*, 8, 650-668,
907 <https://doi.org/10.1002/2015MS000589>, 2016.

908 Mecikalski, J. R., Jewett, C. P., Apke, J. M., and Carey, L. D.: Analysis of Cumulus
909 Cloud Updrafts as Observed with 1-Min Resolution Super Rapid Scan GOES
910 Imagery, *Monthly Weather Review*, 144, 811-830,
911 <https://doi.org/10.1175/MWR-D-14-00399.1>, 2016.

912 Mellado, J. P.: Cloud-top entrainment in stratocumulus clouds, *Annual Review of*
913 *Fluid Mechanics*, 49, 145-169, 10.1146/annurev-fluid-010816-060231, 2017.

914 Menzel, W. P., Smith, W. L., and Stewart, T. R.: Improved cloud motion wind vector
915 and altitude assignment using VAS, *Journal of Applied Meteorology and*
916 *Climatology*, 22, 377-384, [https://doi.org/10.1175/1520-0450\(1983\)022<0377:ICMWWA>2.0.CO;2](https://doi.org/10.1175/1520-0450(1983)022<0377:ICMWWA>2.0.CO;2), 1983.

917 Miltenberger, A. K. and Field, P. R.: Sensitivity of mixed-phase moderately deep
918 convective clouds to parameterizations of ice formation – an ensemble
919 perspective, *Atmos. Chem. Phys.*, 21, 3627-3642,
920 <http://dx.doi.org/10.5194/acp-21-3627-2021>, 2021.

921 Min, Q. L., Li, R., Lin, B., Joseph, E., Wang, S., Hu, Y., Morris, V., and Chang, F.:
922 Evidence of mineral dust altering cloud microphysics and precipitation,
923 *Atmospheric Chemistry and Physics*, 9, 3223-3231,
924 <https://doi.org/10.5194/acp-9-3223-2009>, 2009.

925 Nakajima, T. and King, M. D.: Determination of the optical thickness and effective
926 particle radius of clouds from reflected solar radiation measurements. Part I:
927 Theory, *Journal of Atmospheric Sciences*, 47, 1878-1893,
928 [https://doi.org/10.1175/1520-0469\(1990\)047<1878:DOTOTA>2.0.CO;2](https://doi.org/10.1175/1520-0469(1990)047<1878:DOTOTA>2.0.CO;2), 1990.

929 Noh, Y.-J., Seaman, C. J., Vonder Haar, T. H., and Liu, G.: In situ aircraft
930 measurements of the vertical distribution of liquid and ice water content in
931

932 midlatitude mixed-phase clouds, *Journal of Applied Meteorology and*
933 *Climatology*, 52, 269-279, <https://doi.org/10.1175/JAMC-D-11-0202.1>, 2013.

934 Pavolonis, M. J., Heidinger, A. K., and Uttal, T.: Daytime global cloud typing from
935 AVHRR and VIIRS: Algorithm description, validation, and comparisons,
936 *Journal of Applied Meteorology*, 44, 804-826,
937 <https://doi.org/10.1175/JAM2236.1>, 2005.

938 Pinto, J. O.: Autumnal mixed-phase cloudy boundary layers in the Arctic, *Journal of*
939 *the Atmospheric Sciences*, 55, 2016-2038, [https://doi.org/10.1175/1520-0469\(1998\)055<2016:AMPCBL>2.0.CO;2](https://doi.org/10.1175/1520-0469(1998)055<2016:AMPCBL>2.0.CO;2), 1998.

941 Pscheidt, I., Senf, F., Heinze, R., Deneke, H., Trömel, S., and Hohenegger, C.: How
942 organized is deep convection over Germany?, *Quarterly Journal of the Royal*
943 *Meteorological Society*, 145, 2366-2384, <http://dx.doi.org/10.1002/qj.3552>,
944 2019.

945 Roebeling, R. A., Feijt, A. J., and Stammes, P.: Cloud property retrievals for climate
946 monitoring: Implications of differences between Spinning Enhanced Visible
947 and Infrared Imager (SEVIRI) on METEOSAT-8 and Advanced Very High
948 Resolution Radiometer (AVHRR) on NOAA-17, *Journal of Geophysical*
949 *Research: Atmospheres*, 111, <https://doi.org/10.1029/2005JD006990>, 2006.

950 Rosenfeld, D. and Woodley, W. L.: Deep convective clouds with sustained
951 supercooled liquid water down to -37.5 °C, *Nature*, 405, 440-442,
952 <https://doi.org/10.1038/35013030>, 2000.

953 Rosenfeld, D., Yu, X., Liu, G., Xu, X., Zhu, Y., Yue, Z., Dai, J., Dong, Z., Dong, Y.,
954 and Peng, Y.: Glaciation temperatures of convective clouds ingesting desert
955 dust, air pollution and smoke from forest fires, *Geophysical Research Letters*,
956 38, <https://doi.org/10.1029/2011GL049423>, 2011.

957 Rybka, H., Burkhardt, U., Köhler, M., Arka, I., Bugliaro, L., Görsdorf, U., Horváth, Á.,
958 Meyer, C. I., Reichardt, J., Seifert, A., and Strandgren, J.: The behavior of
959 high-CAPE (convective available potential energy) summer convection in
960 large-domain large-eddy simulations with ICON, *Atmos. Chem. Phys.*, 21,
961 4285-4318, <http://dx.doi.org/10.5194/acp-21-4285-2021>, 2021.

962 Saunders, R., Hocking, J., Turner, E., Rayer, P., Rundle, D., Brunel, P., Vidot, J.,
963 Roquet, P., Matricardi, M., Geer, A., Bormann, N., and Lupu, C.: An update on
964 the RTTOV fast radiative transfer model (currently at version 12), *Geosci.*
965 *Model Dev.*, 11, 2717-2737, <http://dx.doi.org/10.5194/gmd-11-2717-2018>,
966 2018.

967 Schmetz, J., Holmlund, K., Hoffman, J., Strauss, B., Mason, B., Gaertner, V., Koch,
968 A., and Van De Berg, L.: Operational cloud-motion winds from meteosat
969 infrared images, *Journal of Applied Meteorology and Climatology*, 32, 1206-
970 1225, [https://doi.org/10.1175/1520-0450\(1993\)032<1206:OCMWFM>2.0.CO;2](https://doi.org/10.1175/1520-0450(1993)032<1206:OCMWFM>2.0.CO;2), 1993.

972 Schmetz, J., Pili, P., Tjemkes, S., Just, D., Kerkmann, J., Rota, S., and Ratier, A.: An
973 introduction to meteosat second generation (MSG), *Bulletin of the American*
974 *Meteorological Society*, 83, 977-992, [http://dx.doi.org/10.1175/1520-0477\(2002\)083<0977:AITMSG>2.3.CO;2](http://dx.doi.org/10.1175/1520-0477(2002)083<0977:AITMSG>2.3.CO;2), 2002.

976 Seifert, A. and Beheng, K. D.: A two-moment cloud microphysics parameterization
977 for mixed-phase clouds. Part 1: Model description, *Meteorology and*
978 *Atmospheric Physics*, 92, 45-66, <http://dx.doi.org/10.1007/s00703-005-0112-4>,
979 2006.

980 Senf, F., Voigt, A., Clerbaux, N., Hünerbein, A., and Deneke, H.: Increasing
981 resolution and resolving convection improve the simulation of cloud-radiative

982 effects over the North Atlantic, *Journal of Geophysical Research:*
983 *Atmospheres*, 125, e2020JD032667, <https://doi.org/10.1029/2020JD032667>,
984 2020.

985 Sheffield, A. M., Saleeby, S. M., and van den Heever, S. C.: Aerosol-induced
986 mechanisms for cumulus congestus growth, *Journal of Geophysical*
987 *Research: Atmospheres*, 120, 8941-8952,
988 <https://doi.org/10.1002/2015JD023743>, 2015.

989 Sotiropoulou, G., Vignon, É., Young, G., Morrison, H., O'Shea, S. J., Lachlan-Cope,
990 T., Berne, A., and Nenes, A.: Secondary ice production in summer clouds
991 over the Antarctic coast: an underappreciated process in atmospheric models,
992 *Atmos. Chem. Phys.*, 21, 755-771, <https://doi.org/10.5194/acp-21-755-2021>,
993 2021.

994 Stengel, M., Kniffka, A., Meirink, J. F., Lockhoff, M., Tan, J., and Hollmann, R.:
995 CLAAAS: the CM SAF cloud property data set using SEVIRI, *Atmos. Chem.*
996 *Phys.*, 14, 4297-4311, <http://dx.doi.org/10.5194/acp-14-4297-2014>, 2014.

997 Stephens, G. L.: Radiation profiles in extended water clouds. II: Parameterization
998 schemes, *Journal of Atmospheric Sciences*, 35, 2123-2132,
999 [https://doi.org/10.1175/1520-0469\(1978\)035<2123:RPIEWC>2.0.CO;2](https://doi.org/10.1175/1520-0469(1978)035<2123:RPIEWC>2.0.CO;2), 1978.

1000 Stith, J. L., Haggerty, J. A., Heymsfield, A., and Grainger, C. A.: Microphysical
1001 characteristics of tropical updrafts in clean conditions, *Journal of Applied*
1002 *Meteorology*, 43, 779-794, <https://doi.org/10.1175/2104.1>, 2004.

1003 Sullivan, S. C., Barthlott, C., Crosier, J., Zhukov, I., Nenes, A., and Hoose, C.: The
1004 effect of secondary ice production parameterization on the simulation of a cold
1005 frontal rainband, *Atmos. Chem. Phys.*, 18, 16461-16480,
1006 <https://doi.org/10.5194/acp-18-16461-2018>, 2018.

1007 Takeishi, A. and Storelvmo, T.: A study of enhanced heterogeneous ice nucleation in
1008 simulated deep convective clouds observed during DC3, *Journal of*
1009 *Geophysical Research: Atmospheres*, 123, 13,396-313,420,
1010 <https://doi.org/10.1029/2018JD028889>, 2018.

1011 Taylor, J. W., Choullarton, T. W., Blyth, A. M., Liu, Z., Bower, K. N., Crosier, J.,
1012 Gallagher, M. W., Williams, P. I., Dorsey, J. R., Flynn, M. J., Bennett, L. J.,
1013 Huang, Y., French, J., Korolev, A., and Brown, P. R. A.: Observations of cloud
1014 microphysics and ice formation during COPE, *Atmos. Chem. Phys.*, 16, 799-
1015 826, <https://doi.org/10.5194/acp-16-799-2016>, 2016.

1016 Thomas, J., Barrett, A., and Hoose, C.: Temperature and cloud condensation nuclei
1017 (CCN) sensitivity of orographic precipitation enhanced by a mixed-phase
1018 seeder–feeder mechanism: a case study for the 2015 Cumbria flood, *Atmos.*
1019 *Chem. Phys.*, 23, 1987-2002, [10.5194/acp-23-1987-2023](https://doi.org/10.5194/acp-23-1987-2023), 2023.

1020 Twohy, C. H.: Measurements of Saharan dust in convective clouds over the tropical
1021 eastern Atlantic ocean, *Journal of the Atmospheric Sciences*, 72, 75-81,
1022 <https://doi.org/10.1175/JAS-D-14-0133.1>, 2015.

1023 van den Heever, S. C., Carrió, G. G., Cotton, W. R., DeMott, P. J., and Prenni, A. J.:
1024 Impacts of nucleating aerosol on Florida storms. Part I: Mesoscale
1025 simulations, *Journal of the Atmospheric Sciences*, 63, 1752-1775,
1026 <https://doi.org/10.1175/JAS3713.1>, 2006.

1027 Vignon, É., Alexander, S. P., DeMott, P. J., Sotiropoulou, G., Gerber, F., Hill, T. C.
1028 J., Marchand, R., Nenes, A., and Berne, A.: Challenging and improving the
1029 simulation of mid-level mixed-phase clouds over the high-latitude southern
1030 ocean, *Journal of Geophysical Research: Atmospheres*, 126,
1031 e2020JD033490, <https://doi.org/10.1029/2020JD033490>, 2021.

1032 Wan, H., Giorgetta, M. A., Zängl, G., Restelli, M., Majewski, D., Bonaventura, L.,
1033 Fröhlich, K., Reinert, D., Rípodas, P., Kornblueh, L., and Förstner, J.: The
1034 ICON-1.2 hydrostatic atmospheric dynamical core on triangular grids – Part 1:
1035 Formulation and performance of the baseline version, *Geosci. Model Dev.*, 6,
1036 735-763, <http://dx.doi.org/10.5194/gmd-6-735-2013>, 2013.

1037 Zängl, G., Reinert, D., Rípodas, P., and Baldauf, M.: The ICON (ICOsahedral Non-
1038 hydrostatic) modelling framework of DWD and MPI-M: Description of the non-
1039 hydrostatic dynamical core, *Quarterly Journal of the Royal Meteorological*
1040 *Society*, 141, 563-579, <http://dx.doi.org/10.1002/qj.2378>, 2015.

1041 Zhao, B., Wang, Y., Gu, Y., Liou, K.-N., Jiang, J. H., Fan, J., Liu, X., Huang, L., and
1042 Yung, Y. L.: Ice nucleation by aerosols from anthropogenic pollution, *Nature*
1043 *Geoscience*, 12, 602-607, <https://doi.org/10.1038/s41561-019-0389-4>, 2019.

1044 Zhao, X., Liu, X., Burrows, S. M., and Shi, Y.: Effects of marine organic aerosols as
1045 sources of immersion-mode ice-nucleating particles on high-latitude mixed-
1046 phase clouds, *Atmos. Chem. Phys.*, 21, 2305-2327,
1047 <https://doi.org/10.5194/acp-21-2305-2021>, 2021.

1048

1049 **Tables:**

1050

1051 Table 1: Setups of simulations performed in this study.

Num	Experiment	Description
1	$A \times 10^0$ (CTRL)	Without any perturbations, the CTRL run, used as a reference.
2	$A \times 10^{-2}$	INP concentrations for both immersion and deposition mode are scaled by multiplying parameter A in Equation (1) by 10^{-2} .
3	$A \times 10^{-1}$	Same as num. 2, but multiplying by 10^{-1} .
4	$A \times 10^1$	Same as num. 2, but multiplying by 10^1 .
5	$A \times 10^2$	Same as num. 2, but multiplying by 10^2 .
6	$A \times 10^3$	Same as num. 2, but multiplying by 10^3 .
7	$A \times 10^0$ _NSIP	INP concentration as in CTRL. The secondary ice production (rime-splintering process) is switched off.
8	DEC05	Initial and lateral temperature decreases from 3 to 12 km with a maximum increment of 5 K. No perturbations in INPs ($A \times 10^0$).
9	DEC03	Same as num. 8, but with a maximum increment of 3 K.
10	INC03	Initial and lateral temperature increases from 3 to 12 km with a maximum increment of 3 K. No perturbations in INPs ($A \times 10^0$).
11	INC05	Same as num. 10, but with a maximum increment of 5 K.

1052

1053

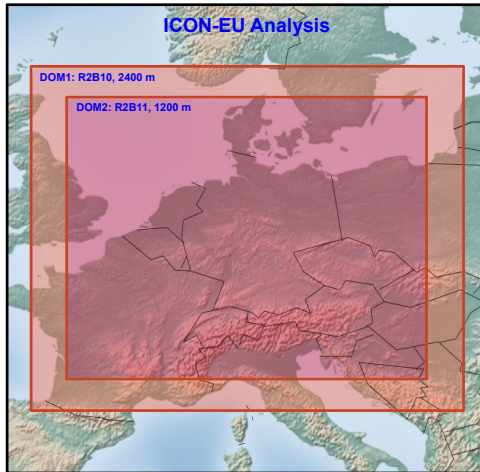
1054

1055

1056 **Figures:**

1057

1058

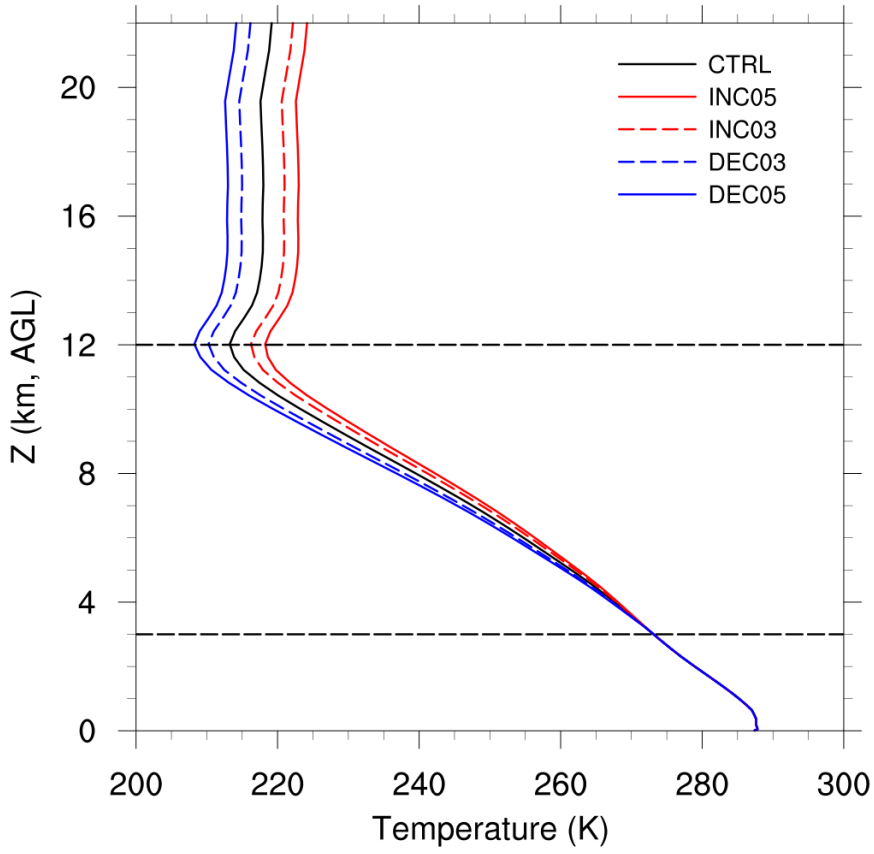


1059

1060 Figure 1: The simulation domains.

1061

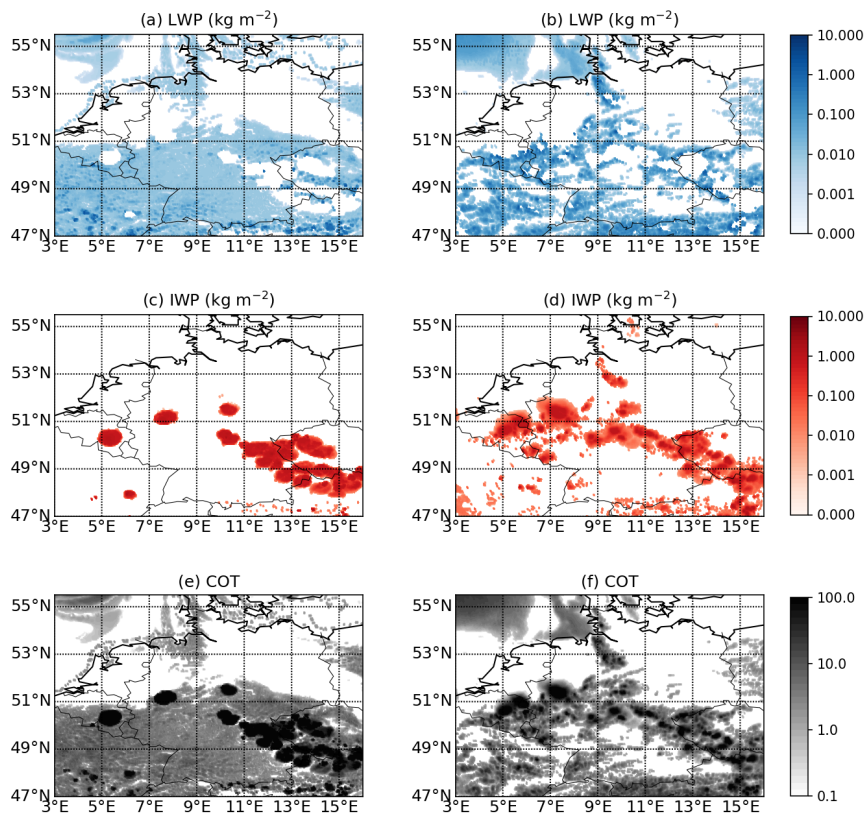
1062



1063

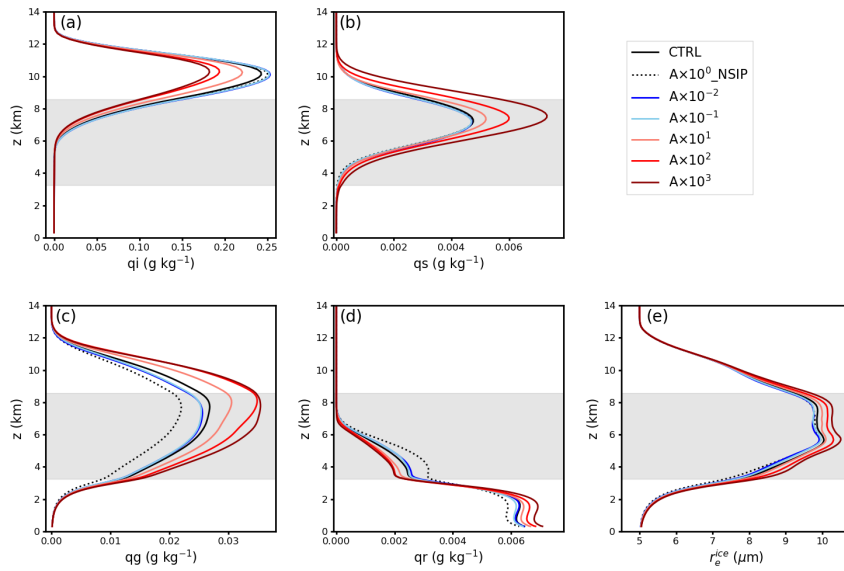
1064 Figure 2: Domain averaged initial temperature profiles. The same modification was
1065 applied to the lateral boundary conditions.

1066



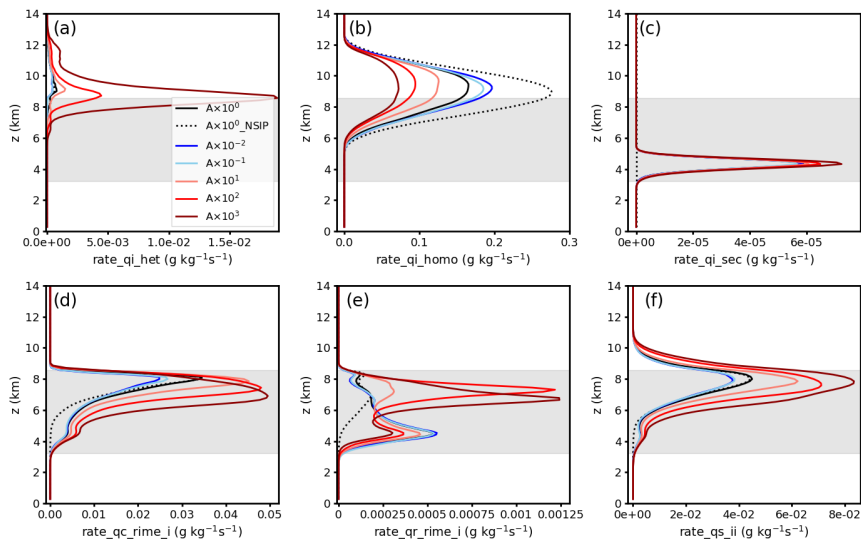
1067
 1068 Figure 3: Spatial distributions of retrieved cloud liquid water path (LWP), ice water
 1069 path (IWP), and cloud optical thickness (COT) at 13:00 UTC. The left panel is for the
 1070 CTRL case (a, c, e) and the right panel is for the CLAAS-2 product (b, d, f).

1071



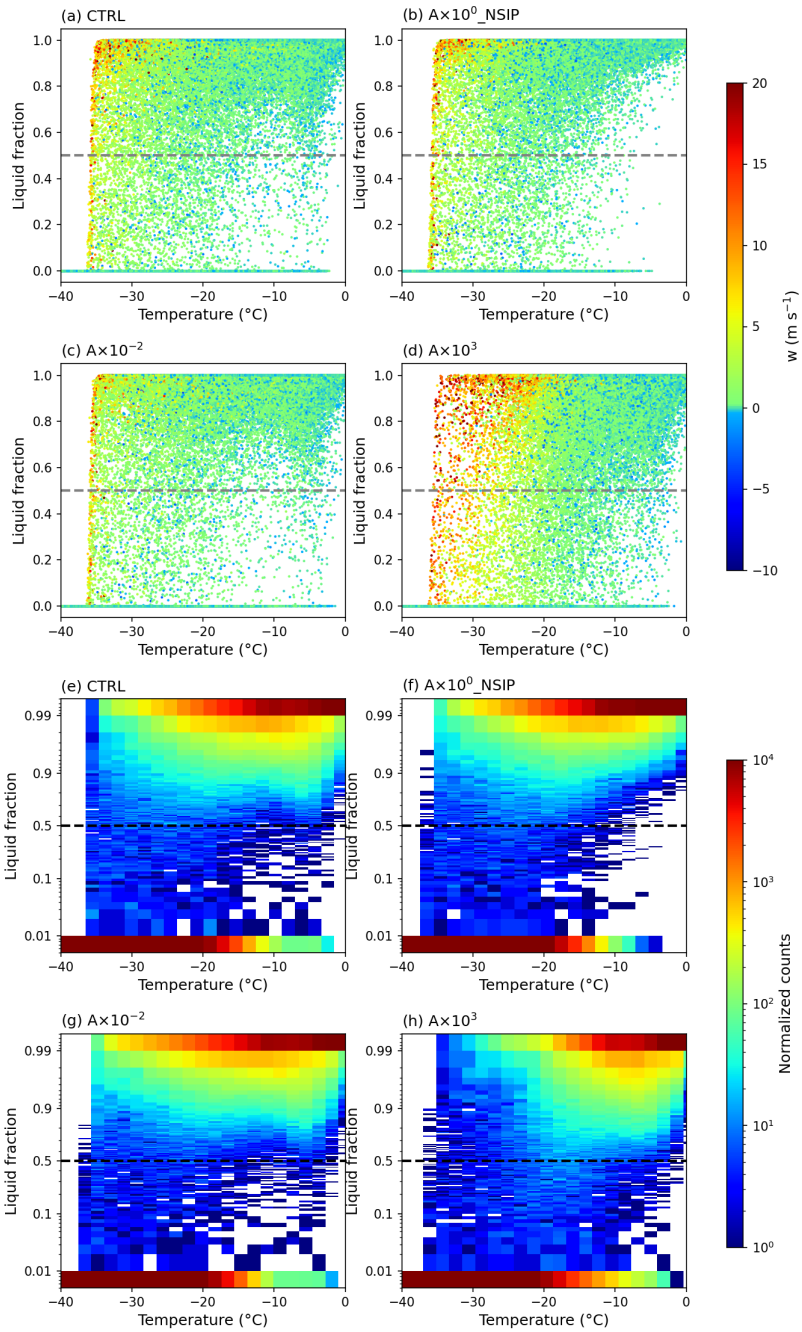
1072
 1073 Figure 4: Spatial- and time-averaged (9:00~19:00) profiles of cloud mass mixing
 1074 ratios of (a) ice crystals, (b) snow, (c) graupel, (d) rainwater, and (e) ice crystal
 1075 effective radius. Mass mixing ratio unit is g kg^{-1} and the unit of ice crystal effective
 1076 radius is μm . Shaded area indicates the spatial- and time-averaged mixed-phase
 1077 region.

1078

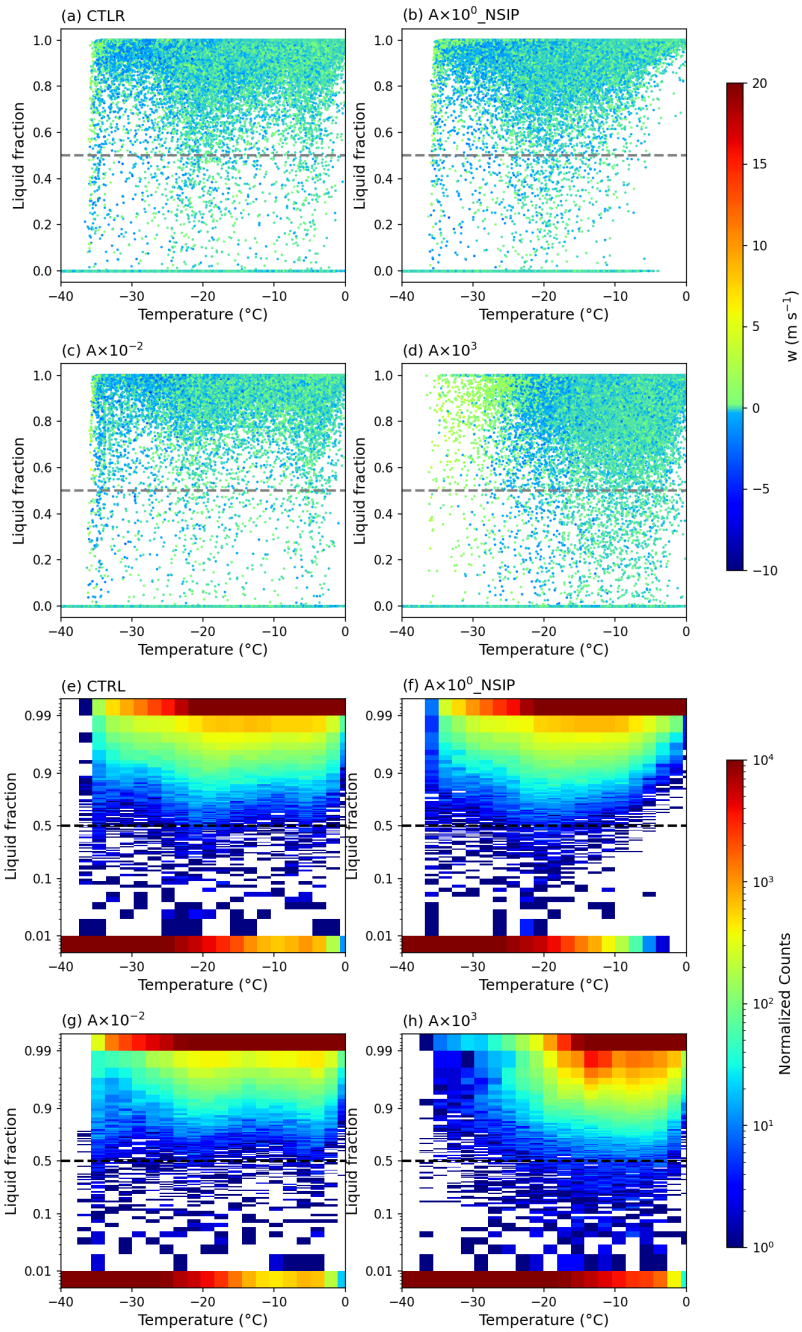


1079
 1080 Figure 5: Spatial- and time-averaged (9:00~19:00) profiles of process rates of (a)
 1081 heterogeneous freezing (immersion and deposition nucleation), (b) homogeneous
 1082 freezing, (c) secondary-ice production (rime-splintering), (d) cloud droplets rimed
 1083 with ice crystals, (e) rain droplets rimed with ice crystals, (f) collection between ice
 1084 and ice. Unit is $\text{g kg}^{-1} \text{s}^{-1}$. The average mixed-phase layer ($0 \sim -38 \text{ }^\circ\text{C}$) is roughly in
 1085 between 3.2 and 8.6 km. Shaded area indicates the spatial- and time-averaged
 1086 mixed-phase region. Unit is $\text{g kg}^{-1} \text{s}^{-1}$.

1087

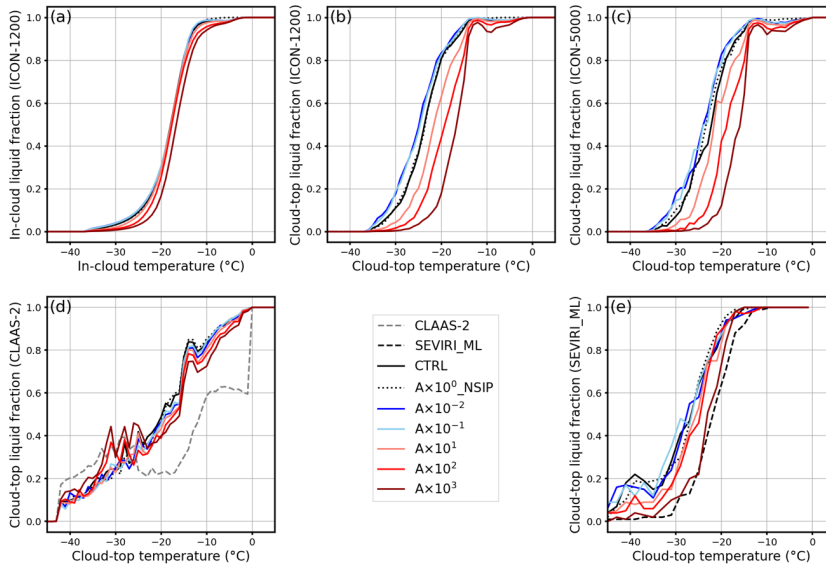


1089 Figure 6: In-cloud supercooled liquid mass fraction distribution as a function of
1090 temperature (binned by 1°C) between 9:00 and 19:00 (a-d) for the 4 cases ($A \times 10^0$,
1091 $A \times 10^0_{\text{NSIP}}$, $A \times 10^{-2}$, $A \times 10^3$), the colour of points indicates the vertical wind velocity
1092 (unit, m s^{-1}). 2-D histogram of in-cloud liquid mass fraction versus temperature (e-f).



1094 Figure 7: Cloud-top supercooled liquid mass fraction distribution as a function of
1095 temperature (binned by 1°C) between 9:00 and 19:00 (a-d) for the 4 cases ($A \times 10^0$,
1096 $A \times 10^0_{\text{NSIP}}$, $A \times 10^{-2}$, $A \times 10^3$), the colour of points indicates the vertical wind velocity
1097 (unit, m s^{-1}). 2-D histogram of cloud-top liquid mass fraction versus temperature (e-f).

1098

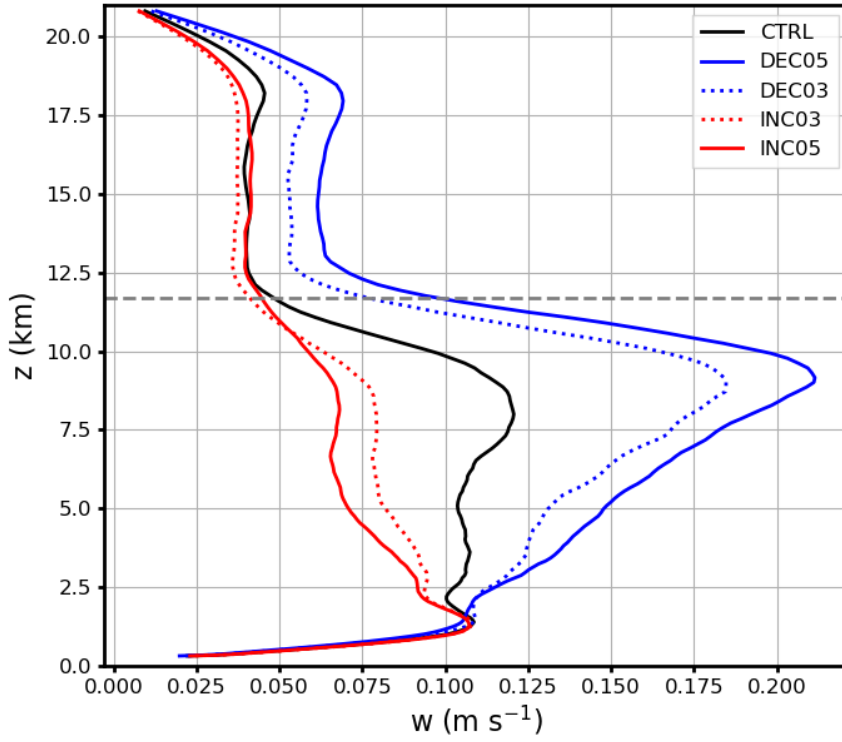


1099

1100 Figure 8: Liquid cloud pixel fraction as a function of temperature from 9:00 to 19:00
1101 UTC for the INP sensitivity experiments, (a) in-cloud fraction calculated from
1102 simulations on ICON native grid (~1200 m), (b) cloud-top fraction calculated from
1103 simulations on ICON native grid (~1200 m), (c) cloud-top fraction calculated from
1104 simulations on SEVIRI's grid (~5000 m), (d) cloud-top fraction calculated by remote-
1105 sensing retrieval algorithms to produce CLAAS-2 dataset, and (e) cloud-top fraction
1106 calculated by remote-sensing retrieval software suite SEVIRI_ML. The temperature
1107 is binned by 1°C in (a), (b), (c), and (d), and by 2°C in (e).

1108

1109



1110

1111

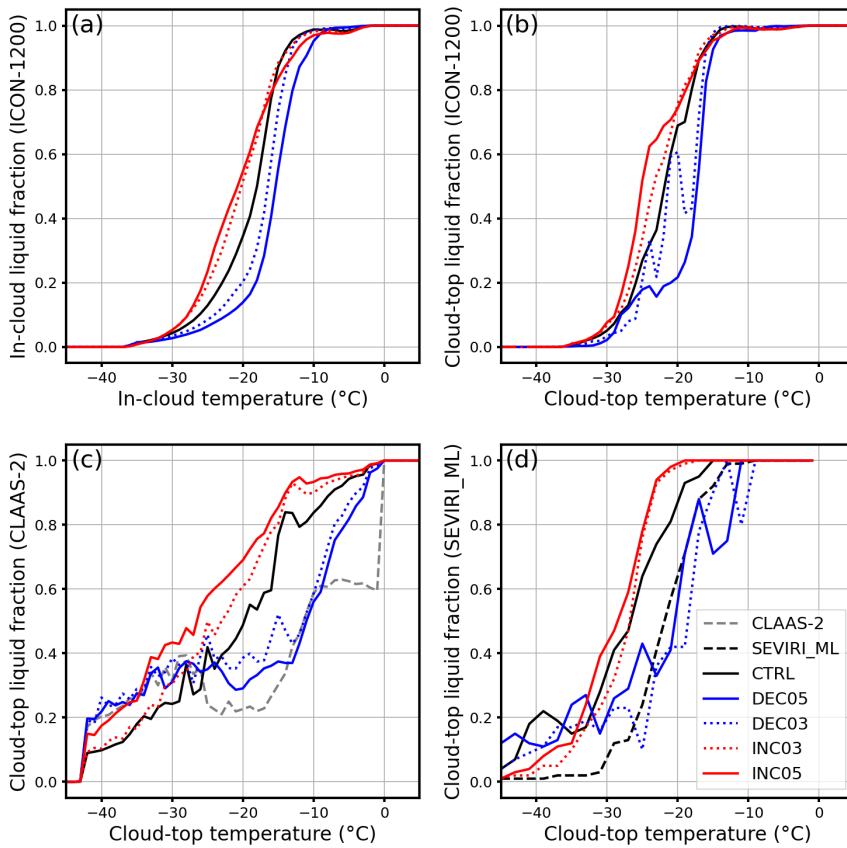
1112

1113

1114

Figure 9: Spatial- and time-averaged (9:00~19:00) profiles of vertical velocities (w values $\leq 0 \text{ m s}^{-1}$ are excluded). The dashed grey line indicates the clout top height which is about 11.7 km.

1115

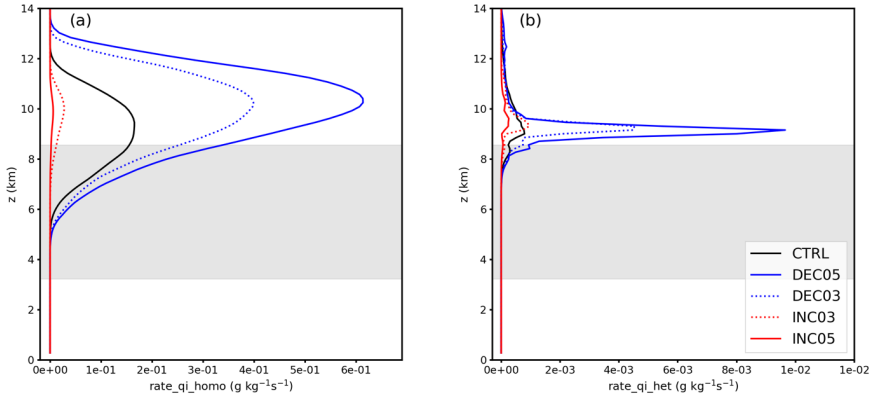


1116

1117 Figure 10: Liquid cloud pixel fraction as a function of temperature from 9:00 to 19:00
1118 for the thermodynamic sensitivity experiments, (a) in-cloud fraction calculated
1119 directly from simulations, (b) cloud-top fraction calculated from directly simulations,
1120 (c) cloud-top fraction calculated by remote-sensing retrieval algorithms to produce
1121 CLAAS-2 dataset, and (d) cloud-top fraction calculated by remote-sensing retrieval
1122 software suite SEVIRI_ML. The temperature is binned by 1°C in (a), (b), and (c), and
1123 by 2°C in (d).

1124

1125



1126

1127 Figure 11: Spatial- and time-averaged (9:00~19:00) profiles of process rates of (a)
1128 homogeneous freezing, (b) heterogeneous freezing (immersion and deposition
1129 nucleation) for cases with perturbed initial thermodynamic states. Shaded area
1130 indicates the spatial and time-averaged mixed-phase region. Unit is $\text{g kg}^{-1} \text{s}^{-1}$.

1131